Bragg glass signatures in Pd_xErTe_3 with X-ray diffraction Temperature Clustering (X-TEC)

Krishnanand Mallayya[1], Joshua Straquadine[2], Matthew Krogstad[3], Maja Bachmann[2],

Anisha Singh[2], Raymond Osborn[3], Stephan Rosenkranz[3], Ian R Fisher[2], Eun-Ah Kim[1]

(Dated: August 1, 2022)

Making progress in studying the interplay between disorder and fluctuations is challenged by the complexity of extracting robust insights from experiments affected by noise and finite resolution. This has hindered observations of the Bragg glass phase, which is predicted to occur in vortex lattices and charge density wave systems in the presence of disorder. Despite its sharp theoretical definition in terms of diverging correlation lengths, establishing the existence of the Bragg glass phase in a charge density wave system has been challenging. Here, we present the first bulk probe evidence of a Bragg glass phase in the systematically disordered CDW material Pd_xErTe_3 using comprehensive x-ray data and a novel machine learning data analysis tool, X-ray Temperature Clustering (X-TEC). Using data from 20,000 Brillouin zones readily analyzed using X-TEC, we establish a diverging correlation length in samples with moderate intercalation over a wide temperature range. To enable such comprehensive analysis, we introduced a new high-through put measure of inverse correlation length: "peak-spread". The detection of Bragg glass order and the resulting phase diagram advance our understanding of the complex interplay between disorder and fluctuations significantly. Moreover, the use of X-TEC to target fluctuations through a high-throughput measure of "peak spread" can revolutionize how the fluctuations are studied in scattering experiments.

INTRODUCTION

The interplay between disorder and fluctuations can result in complex new phases, such as spin glasses, recently celebrated through a Nobel prize [1]. While theoretical frameworks for understanding such complex phases can have far reaching implications, it can be challenging to untangle the subtleties of this interplay from experimental data when finite experimental resolution and noise obscure comparisons with idealized theoretical predictions. The Bragg glass is an example of such an elusive novel phase [2]. It is an algebraically ordered glass, which can appear as ordered as a perfect crystal, but whose Bragg peak intensities diverge as power-laws [3–7]. However, with the experimental resolution cutting off the divergence in actual data, it can be challenging to detect a Bragg glass. While the Bragg glass has been proposed for charge-density-wave systems (CDW) and vortex lattices, unambiguous direct evidence has so far been limited to vortex lattices [8]. Since the lattice periodicity in a vortex lattice is controlled by magnetic field, Klein *et al.* [8] could rely on the magnetic field-independent width of the rocking curve as evidence of the absence of an intrinsic length scale and the underlying algebraic order. However, evidence of Bragg glass phenomena in CDW systems with emergent, system-specific periodicity is suggestive at best and limited to scanning tunneling microscopy (STM) studies of $\mathrm{NbSe_2}$ [9] and $\mathrm{Pd}_x\mathrm{ErTe}_3$ [10]. Hence, whether an algebraically ordered CDW phase can exist as a bulk phase in a CDW system or whether CDW's always respond to disorder as, for example, a vestigial nematic with a short correlation length [11] remains an open problem.

In this work, we present the first evidence using a bulk probe of a Bragg glass phase in a systematically disordered CDW material, $\mathrm{Pd}_x\mathrm{ErTe}_3$, using comprehensive single-crystal x-ray scattering and a novel ML-based method of data analysis called X-ray Temperature Clustering (*X-TEC*) [introduced by some of us in Ref 12]. Specifically, we provide evidence of a vanishing intrinsic length scale by tracking the temperature and momentum dependence of all the CDW peaks in a reciprocal space volume spanning 20000 Brillouin Zones (BZ) with the help of *X-TEC*. To the best of our knowledge, this is the first time CDW fluctuations have been analyzed from more than a handful of peaks. The statistics afforded by such an unprecedented comprehensive analysis of the CDW peak width enables an accurate assessment of CDW correlation lengths by eliminating contributions to the observed peak width from crystal imperfections, and statistically minimizing errors near the resolution limit. The resulting phase diagram establishes the Bragg glass to be the dominant phase, aligning with the onset of the transport anisotropy previously observed [13].

The notion that a quasi-long range ordering of vortex lattices and charge density waves is possible in the form of

Bragg glass in the presence of disorder [2–4] was a surprising theoretical prediction contradicting the long-standing wisdom that order parameters that couple linearly with a disorder potential are destined to be short-ranged at best [14]. The key difference lies in whether the phase fluctuation is allowed to grow indefinitely or the phase is defined compactly within $[0, 2\pi)$. When considering a phase linearly coupling to the disorder potential, Imry and Ma showed that phase fluctuations can grow arbitrarily to overcome the elastic restoring energy, resulting in short-range correlations in dimensions below 4D [14]. However, Nattermann [3] noted that the phase of periodic states such as charge density waves and vortex lattices should be defined compactly within $[0, 2\pi)$; this compactness keeps the impact of the disorder potential in check. Specifically, the disorder-averaged potential energy depends on the exponential of the phase fluctuations, allowing for quasi-long range order in the phase correlations in 3D [2–4] (see Appendix A). Evidence for the divergence of the correlation length with such quasi-long range order would be the vanishing width of structure factor peaks associated with the periodicity[6, 15]. Since the vortex or CDW phase is well-defined within $[0, 2\pi)$ only in the absence of dislocations, observation of such an absence[9, 10] establishes a necessary, but not a sufficient, condition for a Bragg glass.

There are many challenges in making direct observations of Bragg glass phenomena in CDW systems. First, for a systematic understanding of the role of disorder, a material family with adjustable disorder is needed. Second, for a statistically significant separation of real-life issues such as crystal imperfections and finite resolution all contributing to the peak width from the sought-after fluctuation effects, a large volume of comprehensive data is a must. Finally, for a reliable analysis of such large volumes of comprehensive data, a new approach to the data analysis is critical. We turn to $\mathrm{Pd}_x\mathrm{ErTe}_3$ to address the first, material system challenge [10, 13, 16]. Pristine ErTe_3 is a member of the rare earth tritelluride family with nearly square Te nets and a glide plane distinguishing the two in-plane directions a and c [Fig. 1(a)]. It hosts a unidirectional CDW ordering (CDW-1, along c axis) below a critical temperature T_{c1} and an orthogonal unidirectional CDW (CDW-2, along a axis) below T_{c2}, where $T_{c2} < T_{c1}$ due to a weak orthorhombicity [17]. Pd intercalation provides localized disorder potentials at random sites, making $\mathrm{Pd}_x\mathrm{ErTe}_3$ a model system to study emergent phases from suppression of long-range CDW order [10, 13]. Transport measurements in the pristine sample have revealed the onset of anisotropy in resistivity between the a and c axis at the CDW transition temperature [13, 18]. Increasing intercalation lowers the onset temperature for the transport anisotropy [13]. While this reveals the broken C_4 symmetry, two possible candidates for the disordered CDW phase remain open: a short range ordered CDW forming a vestigial nematic phase pinned by weak symmetry-breaking field and a Bragg glass phase characterized by quasi-long range CDW order with divergent power-law correlations.

We overcome the second challenge of the data volume by taking x-ray temperature series data for single crystals $\mathrm{Pd}_x\mathrm{ErTe}_3$ at different intercalation strengths ($x = 0.0,\ 0.5\%,\ 2.0\%,\ 2.6\%,\ 2.9\%$). We utilize highly efficient methods for collecting total x-ray scattering over large volumes of reciprocal space recently developed on Sector 6-ID-D at the Advanced Photon Source [19]. In each measurement, a crystal is rotated continuously through 360°at a rate of 1°/s while images are collected on a fast area detector (Pilatus 2M CdTe) every 0.1 s, with a monochromatic incident x-ray energy of 87 keV. Three rotations are required to fill in gaps between the detector chips. Uncompressed, the raw data volume is over 100 GB. While the data volume is reduced by an order-of-magnitude after transforming the images into reciprocal space meshes, these meshes include over 10,000 Brillouin Zones (BZ) and approximately 5×10^8 bins containing data. Such volumes are collected at a series of temperatures from 30 K to 300 K, controlled by a helium/nitrogen cryostream.

Finally, we overcome the challenge of data analysis through a scalable extraction of theoretically relevant features using a machine learning algorithm *X-TEC* [12]. In the x-ray scattering data, the CDW lattice distortions are manifest as satellite peaks around each of the Bragg peaks [Fig. 1(b)]. We focus on the temperature evolution of three features associated with the CDW peaks [illustrated in Fig.1 (c)]: the peak height, the peak width, and the asymmetry in the intensity distribution between pairs of peaks. In the long-range ordered CDW of the pristine sample, the temperature dependence of peak heights are sufficient to reveal the order parameter and the transition temperature (T_c). However, disorder can often broaden the transition. Moreover, in Bragg glass, the temperature dependence of the peak height does not reveal a clear onset behavior. This is because even after the breakdown of Bragg glass order, a non-vanishing superlattice peak intensity continues to persist to higher temperatures due to short ranged CDWs pinned by disorder [see the first row of the table in Fig. 1(d)]. On the other hand, the peak width of the CDW peaks [Γ in Fig. 1(c)] should vanish upon transition into both the long-range ordered and Bragg glass phases [see the second row of the table in Fig. 1(d)], whereas a short-range ordered phase, such as a vestigial nematic, will show a finite width down to the lowest temperatures (see Appendix-C). Invariably, finite experimental resolution and finite amount of crystalline defects present in samples will mask this difference. However, with enough statistics over a range of temperatures, the temperature dependence of the width can be extrapolated to the vanishing point and allow for the determination of the Bragg glass transition temperature T_{BG} [see the second row in Fig. 1(d)]. Finally, with the peak width vanishing for both the long-range ordered phase and the Bragg glass phase, we need a feature that can distinguish one from the other. We turn to the third and final feature of the asymmetry in the intensity distribution between a pair of CDW satellite peaks [asymmetry in Fig. 1(c)]. Since the intensity difference between two satellite peaks at points $\vec{G} \pm \vec{q}_c$ across the Bragg peak at $\vec{G}$, $I(\vec{G}+\vec{q}_c) - I(\vec{G}-\vec{q}_c)$ is linear on the displacements $\vec{u}_{\vec{q}_c}$ and $\vec{u}_{-\vec{q}_c}$, this difference vanishes without disorder pinning (see Appendix-D) [20]. Hence such asymmetry will distinguish the Bragg glass from long-range order [6, 21] [see the third row in Fig. 1(d)].

Manually tracking the three features of the disordered CDW from large data sets [Fig. 1(e)] presents a daunting challenge, hence the need for an automated machine learning approach like *X-TEC*. At the core of the *X-TEC* algorithm is a Gaussian Mixture Model (GMM) clustering to identify distinct temperature trajectories from the x-ray data. This is achieved by representing the intensity-temperature trajectory at each $\vec{q}$ in reciprocal space: $\{I_{\vec{q}}(T_i)\}$ spanning d number of temperatures $\{T_1, \ldots, T_d\}$ [Fig. 1(e) with $d = 19$], as a point in the d-dimensional space [see SM-Fig.2 for a 2D projection of this space]. From this distribution in hyperspace, GMM identifies a number of distinct clusters and assigns points to each one. From these cluster assignments, we can identify distinct intensity-temperature trajectories present in the data [Fig. 1(g)], thereby revealing the physically interesting ones, such as those representing the temperature dependence of the order parameters.

We first benchmark the *X-TEC* outcomes against known results for the pristine $\mathrm{ErTe_3}$ data [Fig. 2(a)]. The collection of raw data fed into *X-TEC* yields two well-defined CDW transitions in a matter of minutes [see Appendix-F for details on *X-TEC* processing]. From the mean trajectories of the intensities in these two clusters, we can identify two transition temperatures $T_{c1} \approx 260$K and $T_{c_2} \approx 135$K. The transition temperatures identified by *X-TEC* are consistent with those determined from transport anisotropies [13]. Turning to where the clusters are located in reciprocal space, we find that the two intensity clusters correspond to the CDW-1 and CDW-2 peaks, whose K-dependence are consistent with known selection rules [Fig. 2(b-c)]. Both the CDW-1 and CDW-2 peaks are sharp, as expected for 3D CDW order, and therefore satisfy the dimensionality condition necessary for a stable Bragg glass phase [22, 23]. In the rest of the paper, we focus on the CDW-1 peaks with higher transition temperature matching the expectations of the BCS order parameter in the pristine sample [Fig. 2(d)].

Repeating the *X-TEC* analysis on all intercalated samples, one readily extracts our first feature of interest: the temperature trajectory of the CDW peak intensity (peak height) shown in Fig. 2(d,e). We show the average trajectory of all CDW-1 peaks at various intercalation levels. Increasing intercalation suppress the overall intensity of modulations but more importantly it spreads out the intensity distribution as a function of temperature, leaving a long tail up to higher temperatures. The long tail due to pinned CDW fluctuations at the intercalants [24] hinders a clean determination of the putative Bragg glass transition [2–4] from the temperature dependence of the peak intensities. On the other hand, an STM study on $\mathrm{Pd}_x\mathrm{ErTe}_3$ [10] has shown the absence of free dislocations, which is necessary for a Bragg glass, for moderate levels of intercalation ($x \lesssim 2\%$) at a base temperature $\lesssim 1.7$ K.

To target the unambiguous signature of a Bragg glass, we now turn to our second feature of interest, namely the peak width. The objective is to separate three sources of CDW peak broadening with confidence: (1) the instrumental resolution, (2) finite CDW correlation lengths, (3) crystal imperfections. Our approach is to use the $\vec{q} \equiv (H, K, L)$ dependence of the peak broadening since only crystal imperfections would result in a (quadratic) momentum dependence across BZ's (Appendix-E). This strategy requires measuring peak widths over a statistically significant number of BZ's. While our experimental setup can give us ready access to XRD data across 20,000 BZ's, the traditional approach for extracting peak widths cannot use such comprehensive information. Specifically, the traditional peak width extraction approach of fitting a line cut of high-resolution data is not scalable (see SM section G). This forces researchers to an ad-hoc choice of a handful of peaks, ruling out statistically meaningful $\vec{q} \equiv (H, K, L)$ analysis. Instead, we have adopted a high-throughput approach, by combining the automatic *X-TEC* extraction of all the CDW peaks and using a new measure of peak width: the peak *spread*

$$\Gamma_{\vec{q}}(T) \equiv \frac{I_{\vec{q}}^{\mathrm{Tot}}(T)}{I_{\vec{q}}^{\mathrm{Max}}(T)}, \tag{1}$$

in units of the number of pixels. Here, $I_{\vec{q}}^{\mathrm{Tot}}(T)$ is the integrated intensity and $I_{\vec{q}}^{\mathrm{Max}}(T)$ is the maximum intensity (peak height) of the CDW. While being consistent with the conventional peak width estimates [Fig. 2(f), see also Appendix-H], the spread as defined possesses several merits compared to the traditional extraction of the inverse correlation length. First, it is model-independent. Second, it does not require high-resolution data. Third, it naturally integrates with *X-TEC*, which offers the peak boundaries for all the CDW peaks[Fig. 2(e)]. Finally, when combined with *X-TEC*, $\Gamma_{\vec{q}}(T)$ can reveal the momentum and temperature evolution of peak widths over a statistically significant number of CDW peaks.

Armed with the new high-throughput measure "peak-spread" $\Gamma_{\vec{q}}(T)$, we single out the CDW fluctuation contributions by extracting the momentum-independent part of the peak spread by analyzing $\Gamma_{\vec{q}}(T)$ across 20,000 BZ's and the entire temperature range [Fig. 3(a-c)]. Specifically, we fit the momentum dependence of $\Gamma_{\vec{q}}(T)$ at each temperature T to a quadratic function expected in the small $|\vec{q}|$ limit [Fig. 3(b)] [25–29]:

$$\Gamma_{\vec{q}\equiv(H,K,L)}(T) = \Gamma_0(T) + \gamma_H(T)H^2 + \gamma_K(T)K^2 + \gamma_L(T)L^2, \tag{2}$$

where $\gamma_H(T)$, $\gamma_K(T)$, and $\gamma_L(T)$ quantify the momentum dependence at each temperature T along a^*, b^* and c^* axis respectively. In this way, the extracted momentum-independent width $\Gamma_0(T)$ would reflect the peak width solely due to CDW fluctuations. Indeed $\Gamma_0(T)$ extracted from $\sim$ 2000 peaks of the pristine sample drops and plateaus at the critical temperature $T_{\mathrm{c}1}$[Fig. 3(c)], as expected for the long-range order signal cut-off by finite experimental resolution (see Fig. 1(d)).

This analysis reveals the emergence of a threshold temperature in intercalated samples shown in Fig. 3(d-f), below which $\Gamma_0(T)$ becomes constant, signifying that the widths of the CDW peaks at these low temperatures are resolution limited. To go beyond the resolution limit and find the point of vanishing peak width, we extrapolate $\Gamma_0(T)$ using an empirical formula:

$$\Gamma_0(T) = \overline{\Gamma} + \alpha\ (T - \beta)\Theta[T - \beta]. \tag{3}$$

Here, $\Theta[t > 0] = 1$ is the Heaviside step function, and $\overline{\Gamma}$ (the resolution limit), α, and β are the fitting parameters. We estimate the Bragg glass transition temperature to be the positive temperature at which the extrapolation reaches vanishing width, i.e., $T_{BG_1} = \beta - \bar{\Gamma}/\alpha$. We find positive T_{BG_1} defining the Bragg glass phase in all intercalated samples except at the highest concentration [$x = 2.9\%$ in Fig. 3(f)]. Combining the CDW-1 transition temperature T_{c1} of the pristine sample [from Fig. 2(d)] and the newly extracted Bragg glass transition temperature, T_{BG_1} of the intercalated samples, we obtain a comprehensive phase diagram shown in Fig. 3(g). Remarkably, the temperatures identified from the onset of transport anisostropy [13] align closely with the T_{BG_1}, implying that the phase space exhibiting in-plane resistance anisotropy is predominantly covered by the Bragg glass.

Since both long-range order and Bragg glass order have the same signature of a vanishing peak width, we introduce our final feature of interest to distinguish Bragg glass from long range order: the asymmetry between the intensity distribution of a pair of CDW satellite peaks. As it has been long known, disorder pinning of the lattice displacement component $u_{\vec{q}}$ can cause asymmetry between intensities $I(\vec{G}+\vec{q})$ and $I(\vec{G}-\vec{q})$ [6, 20, 21] (see Appendix-D). We probe the asymmetry signature from the surrounding diffuse scattering of the CDW peaks, since the resolution limits the accuracy of asymmetry assessments from the CDW peaks. As shown in Fig. 4(a-b), the contrast between the raw x-ray data from the pristine sample and the intercalated sample is stark. Specifically, while the pristine sample's intensity distribution shows minimal asymmetry of the satellite diffuse scattering across the Bragg peaks, the intercalated sample clearly shows enhanced asymmetry in the form of half diamonds. The raw intensity cuts shown in Fig. 4(c-f), at temperatures spanning the CDW-1 long range ordered and Bragg glass phase for the pristine and intercalated sample respectively, clearly shows that only the intercalated sample in Fig. 4(e-f) exhibit marked asymmetry. The presence of asymmetry specific to the intercalated sample distinguishes it from the pristine sample, and indicates the pinning of CDW modulations by the intercalant-induced disorder. A comprehensive picture of the prevalent asymmetry in the Bragg glass phase emerges upon *X-TEC* clustering shown in Fig. 4(g). When the entire data set of the intercalated sample is split into two clusters (after removing the Bragg peaks and the CDW peaks), the clustering results reveal that the diffuse region around satellite CDW-1 peaks are systematically asymmetric.

In summary, we report the first x-ray scattering evidence of the Bragg glass phase in a family of disordered charge density wave systems, Pd-intercalated $\mathrm{ErTe_3}$. In order to disentangle intrinsic phase fluctuation effects of the CDW from crystalline imperfections despite finite experimental resolution, we obtained comprehensive XRD data spanning $\sim 20,000$ Brillouin zones over 30-300K range of temperatures. We then analyzed the entire ∼150GB of XRD data using *X-TEC*, an unsupervised machine learning tool for revealing collective phenomena from voluminous temperature dependent XRD data[12]. We employed a multi-faceted approach of tracking three features, namely the peak height, the peak width, and the peak asymmetry, throughout the entire dataset. Consolidating the results of this analysis, we were able to disentangle the effects of lattice imperfections and finite momentum resolution from the intrinsic tendency for topological quasi-long range order into a Bragg glass phase. Thus we discovered that the Bragg glass phase spans most of the phase space that exhibits transport anisotropy, extending up to remarkably high temperatures.

The significance of our findings are two-fold. Firstly, we made significant advances in understanding the elusive Bragg glass phase by establishing direct evidence of the Bragg glass for the first time in a charge density wave systems and mapping out the transition temperature T_{BG}. It is remarkable that the Bragg glass phase suggested from the STM measurements only at temperatures below 1.7K extends all the way up to 100K and beyond until the Bragg glass phase collapses at around 2.9% intercalation. Moreover, the evidence for the Bragg glass we established leaves only a very narrow range of phase space that can possibly support the competing short-range ordered phase. Secondly, the new discovery enabled by the use of *X-TEC* and the new high-throughput measure of peak-width demonstrates the potential of the new ML-enabled data analysis in addressing fundamental issues when intrinsic fluctuations and the effect of disorder lead to a complex and rich plethora of phenomena. The high-throughput measure of peak width enabled us to disentangle the effects of crystalline defects from the effects of intrinsic CDW phase fluctuations by giving us access to zone-to-zone correlation in fluctuations over 20,000 BZ's. This separation in turn allowed us to connect the voluminous XRD data with the STM observations and the theory of Bragg glasses. The modality of comprehensive high-throughput extraction of theoretically inspired features promises to enable new discoveries in the era of big data, rich with information, and connect varied facets of complex systems accessible to different probes.

Acknowledgements: This work was supported by the U.S. Department of Energy, Office of Basic Energy Sciences, Division of Materials Sciences and Engineering and used resources of the Advanced Photon Source, a U.S. Department of Energy Office of Science User Facility at Argonne National Laboratory. The initial *X-TEC* analysis on the pristine sample was carried out on the Red Cloud at the Cornell University Center for Advanced Computing, with the support of the DOE under award DE-SC0018946. The *X-TEC* analysis on intercalated samples were carried out on the high powered computing cluster funded in part by the Gordon and Betty Moore Foundation's EPiQS Initiative, Grant GBMF10436 to E-AK and by the New Frontier Grant from the college of Arts and Sciences at Cornell to E-AK. Work at Stanford University (crystal growth and characterization, and contributions to the diffraction experiments) was supported by the Department of Energy, Office of Basic Energy Sciences, under contract DE-AC02-76SF00515.

FIGURES

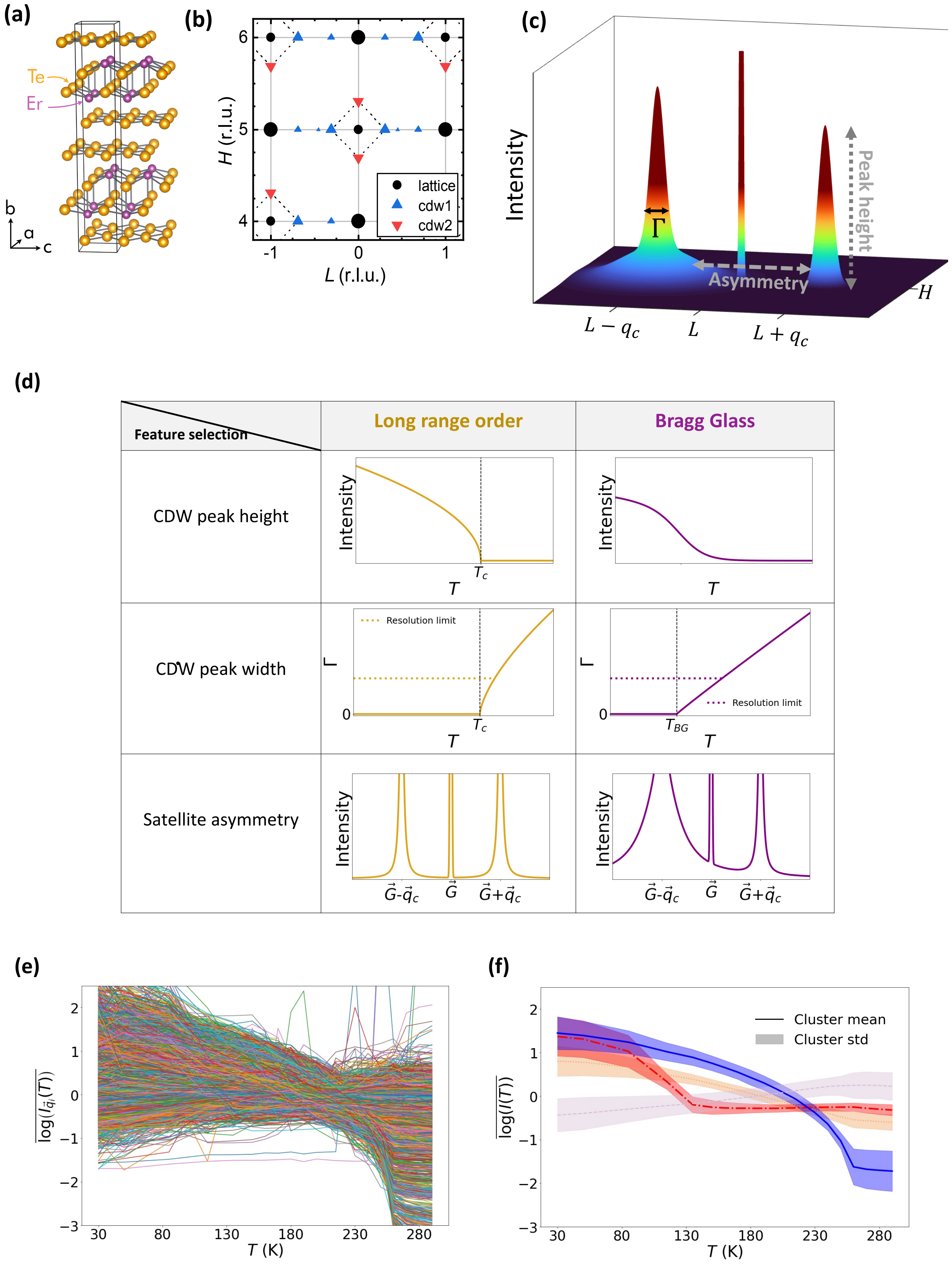
(a)
Te
Er
b
a
c
(b)
6
5
4
H (r.l.u.)
-1
0
1
L (r.l.u.)
lattice
cdw1
cdw2
(c)
Intensity
Γ
Peak height
Asymmetry
$L-q_c$
L
$L+q_c$
H
(d)
Feature selection
Long range order
Bragg Glass
CDW peak height
Intensity
T_c
T
CDW peak width
Resolution limit
Γ
0
T_{BG}
Satellite asymmetry
$\vec{G}$-$\vec{q}_c$
$\vec{G}$
$\vec{G}$+$\vec{q}_c$
(e)
$\overline{\log(I_{\vec{q}_i}(T))}$
2
1
0
−1
−2
−3
30
80
130
180
230
280
T (K)
(f)
$\overline{\log(I(T))}$
Cluster mean
Cluster std

Fig 1: **(a):** The crystal structure of pure ErTe_3. The Te planes have approximately square geometry. The crystal belongs to the $Cmcm$ space group, b denotes the out-of-plane axis, and a, c are the in-plane axes. **(b):** A schematic [13] showing the Bragg peaks (circles) and CDW peaks (triangles) in the in-plane (a^*-c^*) reciprocal space. The CDW-1 (up triangle) and CDW-2 (down triangle) satellite peaks are aligned along the c^* and a^* axes, respectively. **(c):** Schematic for the in-plane (a^*-c^*) intensity distribution of the pair of CDW satellite peaks [at $(H, L \pm q_c)$] around a Bragg peak [at (H, L)], with the three features of interest: the height of the peak (vertical dotted arrow), the width of the peak Γ (solid arrow), and the asymmetry between the satellite peaks (dashed arrow). **(d):** Table summarising the diagnostics for classifying the three phases. The first row describes the CDW intensity (peak height) temperature trajectory. Only the pristine sample with long range order exhibits a sharp onset, marking the transition temperature T_c. On the other hand, even after the breakdown of Bragg glass order upon increasing temperature, short ranged fluctuations persist (due to disorder pinning) and contribute to the peak height. This obscures the identification of the Bragg glass transition. The second row illustrates the temperature dependence of the CDW peak width Γ. The width is zero in the long-range ordered phase below T_c of the pristine sample, as well as in the Bragg glass phase below the transition temperature T_{BG_1} of the disordered sample (Appendix-B). The observed width levels off at the resolution limit (dotted line) at temperatures above T_c and T_{BG_1}. The third row illustrates the asymmetry in the intensity distribution across a Bragg peak. The asymmetry is absent in the pristine sample, and its presence in the disordered sample indicates disorder pinning (Appendix-C). **(e,f):** An illustration of *X-TEC* to cluster distinct intensity-temperature trajectories, $I(T)$, given the intensity-temperature trajectory $\{I_{\vec{q}}(T)$ of the pristine ErTe_3 sample at various momenta $\vec{q}$ in the reciprocal space. The raw trajectories at each $\vec{q}$ are rescaled as $\overline{\log[I_{\vec{q}}(T)]} = \log[I_{\vec{q}}(T)] - \langle \log[I_{\vec{q}}(T)] \rangle_T$ [panel (e)]. The *X-TEC* clusters the trajectories (with color assignments to identify each cluster). The distinct trajectories $I(T)$ and their standard deviation are shown in panel (f).

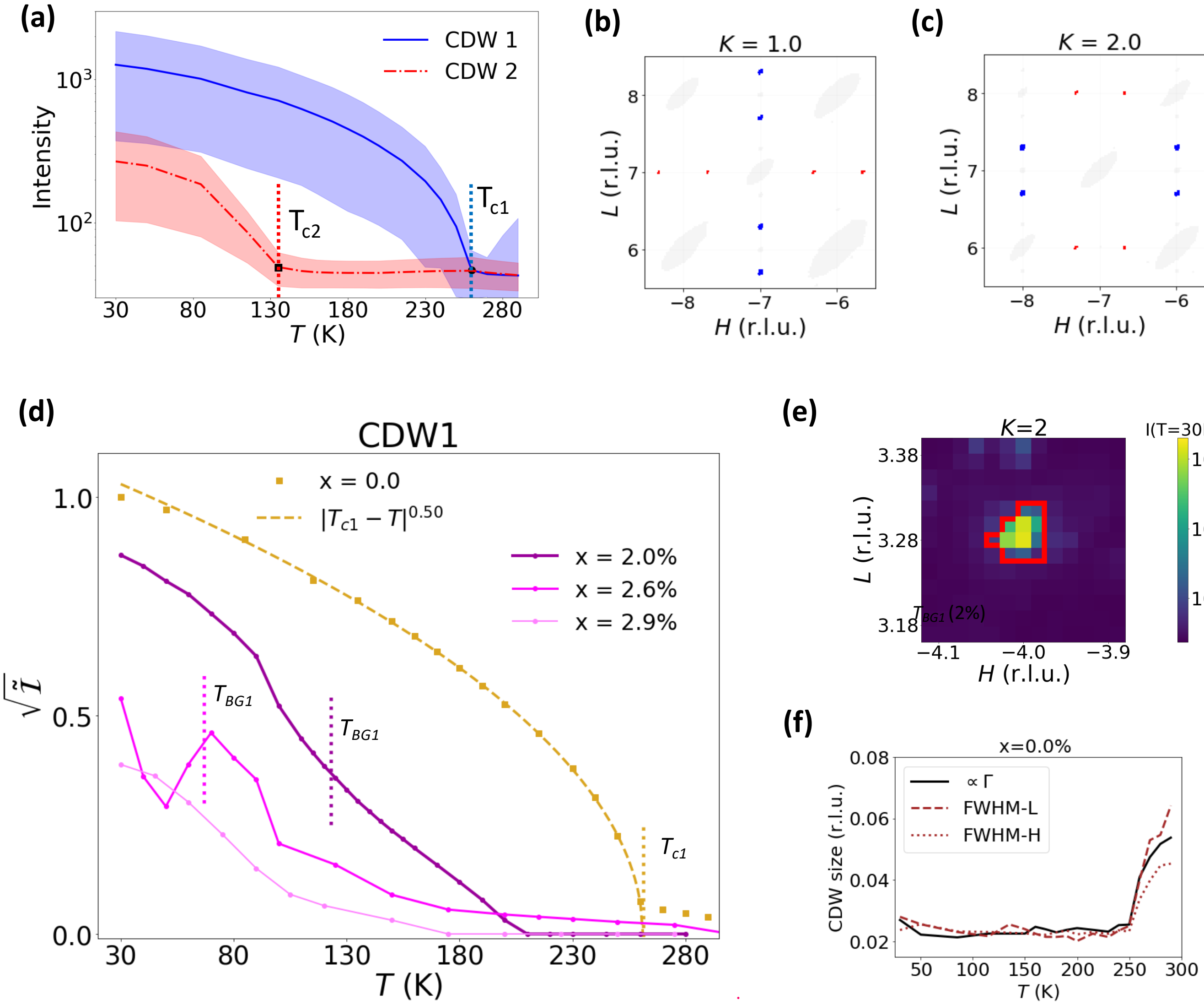
(a)
Intensity
10^3
10^2
CDW 1
CDW 2
T_{c2}
T_{c1}
30
80
130
180
230
280
T (K)
(b)
K = 1.0
L (r.l.u.)
H (r.l.u.)
−8
−7
−6
8
7
6
(c)
K = 2.0
L (r.l.u.)
H (r.l.u.)
−8
−7
−6
8
7
6
(d)
CDW1
$\sqrt{\tilde{I}}$
1.0
0.5
0.0
x = 0.0
$|T_{c1} - T|^{0.50}$
x = 2.0%
x = 2.6%
x = 2.9%
T_{BG1}
T_{BG1}
T_{c1}
30
80
130
180
230
280
T (K)
(e)
K=2
I(T=30K)
10^4
10^3
10^2
L (r.l.u.)
3.38
3.28
3.18
T_{BG1} (2%)
−4.1
−4.0
−3.9
H (r.l.u.)
(f)
x=0.0%
CDW size (r.l.u.)
0.08
0.06
0.04
0.02
∝ Γ
FWHM-L
FWHM-H
50
100
150
200
250
300
T (K)

Fig 2: (a): Benchmarking the *X-TEC* analysis of the scattering intensities of pristine $\mathrm{ErTe_3}$. *X-TEC* reveals the intensity clusters corresponding to the two CDW order parameter trajectories, color-coded as red and blue. The lines describe the mean and the shaded regions describe one standard deviation of the intensities within each cluster. The estimated transition temperatures $T_{c1} \approx 261K$ for CDW-1 and $T_{c_2} \approx 135K$ for CDW-2 are consistent with the temperatures from transport measurements in Ref. 13. **(b-c):** A small region of reciprocal space where momenta whose intensity trajectory belong to the red and blue cluster assignments in (a) are labeled as red and blue pixels respectively. The red (blue) pixels conform to the CDW-1 (CDW-2) peaks along c^* (a^*) axis. The light grey pixels correspond to Bragg peaks and their diffuse scattering. The 3D structure of the peaks are apparent from the $k = 1$ (odd) plane (panel (b)) and $k = 2$ (even) plane (panel (c)) that show two different patterns reflecting the *Cmcm* selection rules governing the Bragg peaks. **(d):** The CDW-1 peak averaged intensity (peak height) for $\mathrm{Pd}_x\mathrm{ErTe_3}$ at intercalation strength $x = 0$, 2.0%, 2.6% and 2.9%. The $\tilde{I}$ is obtained from the average of all the intensities in the CDW-1 cluster ($\sim$ 2000 peaks), from which we subtract the background intensity contribution ($\tilde{I}$ below the background floor are set as zero). The $\tilde{I}$ for all samples are normalized with the maximum value from $x = 0$, for comparison. $\sqrt{\tilde{I}(T)}$ for $x = 0$ fits well to a power law $\propto (T_{c1} - T)^{\beta}$ giving $T_{c1} \sim 261$K (star symbol) and $\beta = 0.502$ matching the BCS order parameter exponent. The Bragg glass transition temperature T_{BG_1} for $x = 2\%$ and $x = 2.6\%$ is estimated from the peak width analysis in Fig. 3(e-f). All solid lines are guides to the eyes. **(e):** A CDW-1 peak intensity distribution in the H-L plane ($K = 2$) for the $x = 0\%$ sample at $T = 30$K. The red boundary for the CDW-1 peak is estimated by *X-TEC* (pixels inside the boundary belong to CDW-1 cluster). Within this boundary, the total intensity $I^{\mathrm{Tot}}_{\vec{q}}(T)$ and maximum intensity $I^{\mathrm{Max}}_{\vec{q}}(T)$ of the peak gives the high throughput measure of peak spread $\Gamma_{\vec{q}}(T)$ [Eq. (1)]. **(f):** The peak spread (Γ) of the CDW peak in (e), along with the FWHM from line cuts along H (FWHM-H) and L (FWHM-L), at various T for $x = 0\%$.

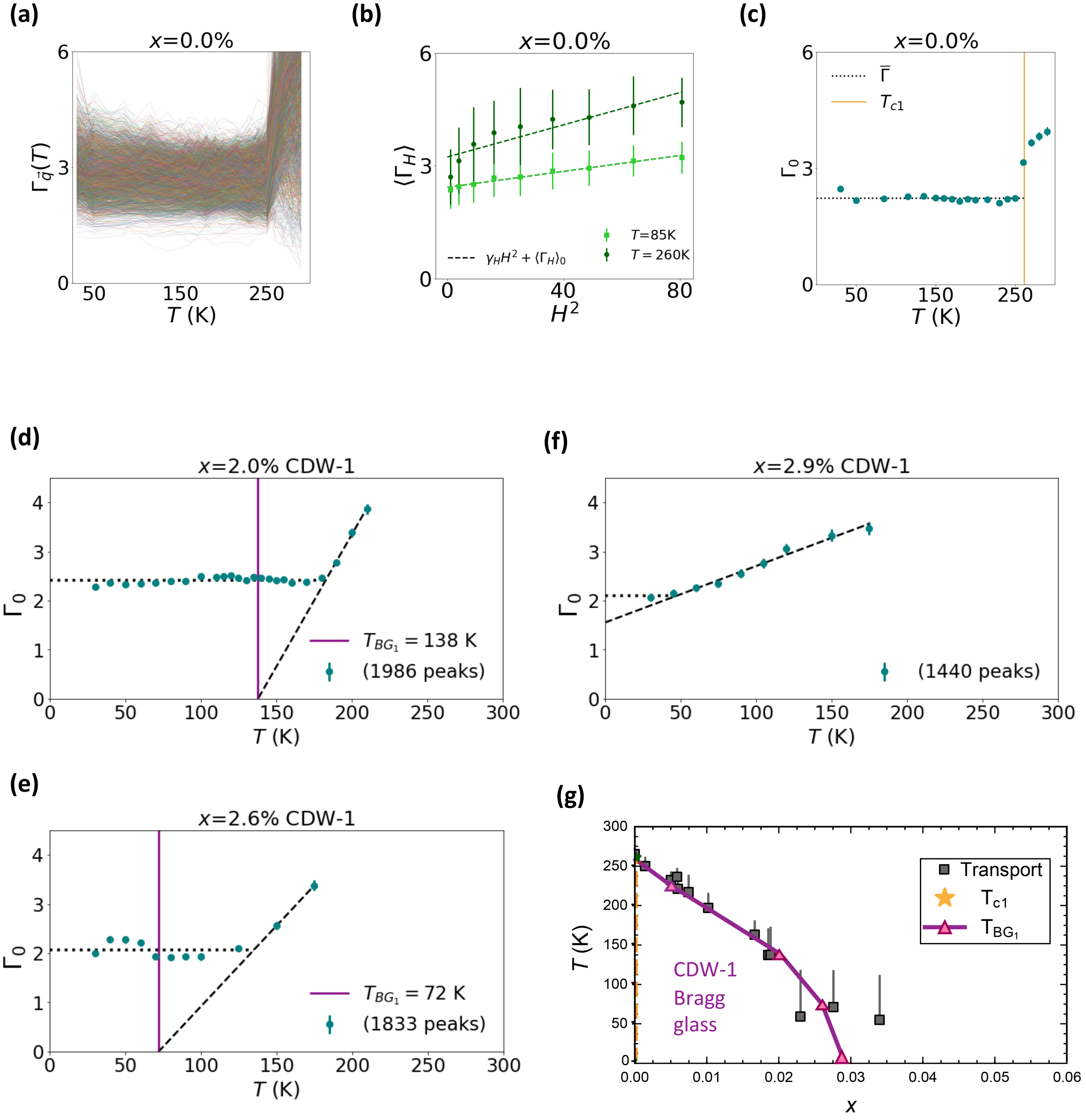
(a)
x=0.0%
$\Gamma_{\vec{q}}(T)$
6
3
0
50
150
250
T (K)
(b)
x=0.0%
$\langle\Gamma_H\rangle$
6
3
0
0
40
80
H^2
$\gamma_H H^2 + \langle\Gamma_H\rangle_0$
T=85K
T = 260K
(c)
x=0.0%
Γ_0
6
3
0
50
150
250
T (K)
$\overline{\Gamma}$
T_{c1}
(d)
x=2.0% CDW-1
Γ_0
4
3
2
1
0
0
50
100
150
200
250
300
T (K)
$T_{BG_1} = 138$ K
(1986 peaks)
(f)
x=2.9% CDW-1
Γ_0
4
3
2
1
0
0
50
100
150
200
250
300
T (K)
(1440 peaks)
(e)
x=2.6% CDW-1
Γ_0
4
3
2
1
0
0
50
100
150
200
250
300
T (K)
$T_{BG_1} = 72$ K
(1833 peaks)
(g)
T (K)
300
250
200
150
100
50
0
0.00
0.01
0.02
0.03
0.04
0.05
0.06
x
Transport
T_{c1}
T_{BG_1}
CDW-1
Bragg
glass

Fig 3: **(a):** Peak spread $\Gamma_{\vec{q}}(T)$ of all CDW-1 peaks in the $x = 0$ data. **(b):** The quadratic momentum (H^2) dependence of $\Gamma_{\vec{q}}(T)$. $\langle \Gamma_H \rangle$ (symbols) is obtained by averaging $\Gamma_{\vec{q}}$ over values of K and L that share the same $|H|$. The error bars indicate the standard deviation. **(c):** From the erratic and broad distribution of $\Gamma_{\vec{q}}(T)$ in panel (a), the momentum-independent spread Γ_0 extracted from the 3D quadratic fit [Eq. (2)] shows a T independent (resolution limited) spread below T_{c1} [$T_{c1} = 261$ K from Fig. 2 (d)]. Error bars on the symbols are 95% confidence bounds on Γ_0. **(d-f):** The $\vec{q}$ independent broadening of CDW-1 peak spread, $\Gamma_0(T)$, extracted from $\sim$ 2000 peaks by fitting their $\Gamma_{\vec{q}}$ to a quadratic function of $\vec{q}$ [Eq. (2)] for $x = 2\%$, 2.6%, and 2.9% in panels (d), (e) and (f) respectively. Error bars indicate 95% confidence bounds. Dashed lines are a phenomenological fitting function [Eq. (3)] to extract CDW-1 Bragg glass temperature T_{BG_1}. The dotted lines mark the resolution limit $\overline{\Gamma}$ from the fit. We find a Bragg glass regime for $x = 2\%$ and 2.6% sample by extracting T_{BG_1} (vertical solid lines) from extrapolating the broadening regime to zero spread. **(g):** Our estimates for the transition temperatures T_{c1} of $x = 0\%$ (star symbol) and T_{BG_1} of $x > 0$ (up triangle symbols) are overlaid on the phase diagram from the in-plane resistance anisotropy measurements (square symbols) from Ref. 13. Lines are guides to the eyes. The CDW-1 long range ordered phase of $x = 0\%$ is indicated by the dashed orange line, and the CDW-1 Bragg glass phase lies below T_{BG_1} for $x > 0$.

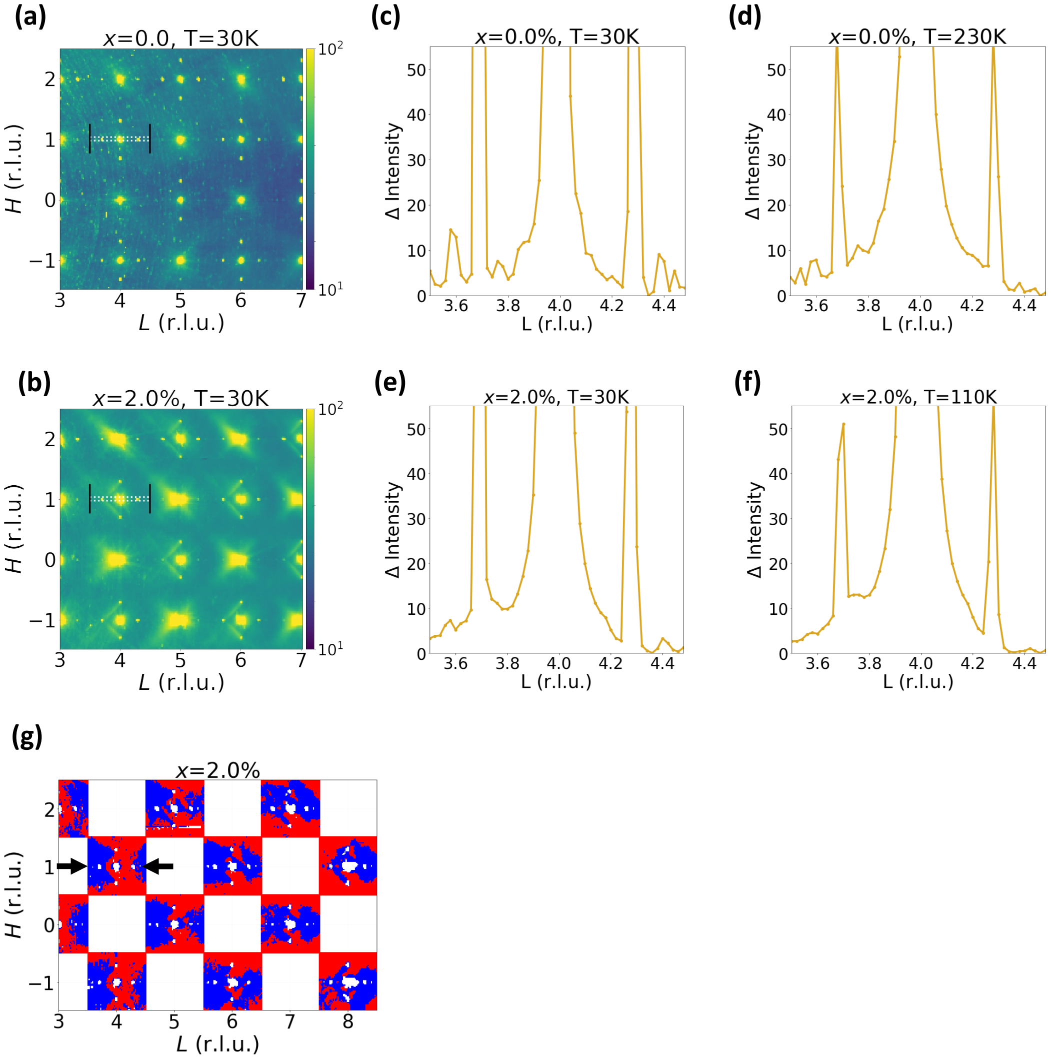
(a)
x=0.0, T=30K
H (r.l.u.)
L (r.l.u.)
10^2
10^1
(b)
x=2.0%, T=30K
(c)
x=0.0%, T=30K
Δ Intensity
L (r.l.u.)
(d)
x=0.0%, T=230K
(e)
x=2.0%, T=30K
(f)
x=2.0%, T=110K
(g)
x=2.0%

Fig 4: Intensity asymmetry of the CDW satellite peaks. **(a-b):** The x-ray intensity at $T = 30$K, in the H-L plane with K (out-of-plane axis) averaged over all integers ($-20 \leq K \leq 20$), for the pristine sample [$x = 0\%$ in panel(a)] and intercalated sample [$x = 2\%$ in panel (b)]. Only the intercalated sample shows a diffuse scattering that is asymmetrically distributed between the two satellite peaks, in the form of half diamonds. The white horizontal lines across a pair of CDW-1 satellite peaks mark the region along which a line cut is taken and is shown in panels (c-f). Line cuts are along $3.5 \leq L \leq 4.5$ (r.l.u) with intensity averaged over $H = 1 \pm 0.02$ (r.l.u) and over all integer values of $K \in [-20, 20]$. **(c-d):** Line cut of the intensity $I(L)$ for the pristine sample at 30K (panel c) and 230K $< T_{c1}$ (panel d). **(e-f):** Line cut of the intensity $I(L)$ for the $x = 2\%$ intercalated sample at 30K (panel e) and at 110K $< T_{BG1}$ (panel f). The asymmetry is clearly visible in the line cuts of the intercalated sample (and absent in the pristine sample) at both the temperatures. **(g):** Two cluster *X-TEC* results color coded as red and blue, from the temperature trajectories of the diffuse scattering intensities of the $x = 2\%$ intercalated sample. Only the temperature trajectories below T_{BG1} are clustered. The pixels are colored red (blue) if their intensity trajectory belongs to the red (blue) cluster. The asymmetric distribution of red and blue clusters surrounding the CDW satellite peaks (see black arrows for reference) is systematically present in the intercalated sample in the Bragg glass phase, clearly revealing the signature of disorder pinning. The intensities of the CDW peaks and $H+L =$ odd Bragg peaks (white pixels, identified from a prior *X-TEC* analysis) are excluded from this two-cluster *X-TEC*, along with the $H+L =$ even Bragg peaks removed by a square mask (square white regions).

Appendix A : Scaling argument for Bragg glass

The energy scaling argument by Imry and Ma considering an XY model [14], and by Fukuyama and Lee considering a disordered CDW [30], indicates that only short ranged correlations are allowed in continuous symmetry broken states below 4 dimensions, based on an assumption of a disorder potential linearly coupled to the phase. However for the CDW, the true potential is non-linear and a periodic function of phase. Nattermann [3] took this periodicity into account and showed that the modified scaling argument supports the quasi-long range order of the Bragg glass. Here we recall the scaling arguments, starting with Imry and Ma's analysis and its shortcoming, and then follow Nattermann's analysis [Ref. 3] supporting the Bragg glass order in 3D. We start with a charge density wave,

$$\rho(\vec{r},\phi) = \rho_0 \cos[\vec{q}_c \cdot \vec{r} + \phi(\vec{r})] \tag{4}$$

with an incommensurate wave vector $\vec{q}_c$, a constant amplitude ρ_0 and a phase $\phi(\vec{r})$ that can spatially vary due to thermal fluctuations and disorder interactions. The interaction with quenched disorder in D spatial dimensions can be described with an elastic model whose Hamiltonian is given by [7],

$$H = \frac{C}{2}\int d^D r\ |\vec{\nabla}\phi(\vec{r})|^2 + V_0 \int d^D r\ \Sigma(\vec{r})\rho(\vec{r},\phi) \tag{5}$$

where the first term is the elastic part with C as the elastic stiffness, and the second term is the disorder potential due to quenched impurities exerting a potential V_0 on the charge density, and distributed with a probability density $\Sigma(\vec{r})$. We assume there are no topological defects in the system so that $\phi(\vec{r})$ is single valued and the elastic model is well defined, which is a necessary condition for a Bragg glass [2, 5, 31]. A spatially modulated phase $\phi(\vec{r})$ increases the elastic energy, but can lower the potential energy by conforming $\rho(\vec{r})$ to the impurity distribution. The disordered phases arise from this competition between the elastic energy cost and the potential energy gain. These phases are distinguished by the fluctuations in $\phi(\vec{r})$ relative to an arbitrary reference point $\phi(\vec{r}=0)$, given by

$$W^2(|\vec{r}|) = \overline{\langle(\phi(\vec{r}) - \phi(0))^2\rangle} \tag{6}$$

where $\langle \dots \rangle$ denotes a thermal average and $\overline{(\dots)}$ denotes a disorder ensemble average. To simplify, we fix $\phi(0) = 0$, and assume that fluctuations are spherically symmetric with respect to $\vec{r} = 0$.

We first identify the scaling of elastic energy cost from Eq. (5). For a phase that varies by an amount $W(R)$ over a distance R, the elastic energy (EE) in the volume R^D scales as

$$\text{EE} \propto \frac{1}{2} C \left(\frac{W(R)}{R}\right)^2 R^D \tag{7}$$

This shows that for $D > 2$, the elastic energy cost increases with phase fluctuations over larger distances. In the absence of disorder, this energy cost protects the long range order.

Now we discuss the scaling of the potential energy in a volume R^D. We imagine each site is independently occupied by an impurity with probability n_I, the impurity concentration. The volume includes $n_I R^D$ impurities, and each random impurity site $\vec{r}_i$ contributes a potential energy $V(\vec{r}_i)$ given by,

$$V(\vec{r}_i) = V_0\rho_0 \cos[\vec{q}_c.\vec{r}_i + \phi(\vec{r}_i)] \tag{8}$$

Imry-Ma scaling: Imry and Ma's argument is valid when $\phi(\vec{r}_i)$ is small and a linear approximation applies to Eq. (8), given by

$$V(\vec{r}_i) = V_0\rho_0 \left(\cos(\vec{q}_c \cdot \vec{r}_i) - \sin(\vec{q}_c \cdot \vec{r}_i)\phi(\vec{r}_i)\right) + \mathcal{O}(\phi^2(\vec{r}_i)) \tag{9}$$

where we can discard the first term that sets a constant offset, and the second term gives the potential energy gain from $\phi(\vec{r}_i)$. To estimate the magnitude of this energy gain in a volume R^D, we note that a typical impurity site has a position $|\vec{r}_i| \sim R$ and the phase $|\phi(\vec{r}_i)| \approx \left(\overline{\langle\phi^2(\vec{r}_i)\rangle}\right)^{1/2} \sim W(R)$. Hence, the magnitude of potential energy gain from each impurity, $V_0\rho_0 \left|\sin(\vec{q}_c \cdot \vec{r}_i)\phi(\vec{r}_i)\right|$, has a typical value $\sim V_0\rho_0 W(R)$, and the magnitude of total potential energy (PE) scales as

$$\mathrm{PE} \sim \left(\sqrt{n_I R^D}\right) V_0\rho_0 W(R) \tag{10}$$

where the factor $\sqrt{n_I R^D}$ follows from central limit theorem giving the root mean squared value from $n_I R^D$ independent random impurities.

Equating the elastic energy cost [Eq. (7)] to potential energy gain [Eq. (10)] gives the optimal $W(R)$ given by

$$C R^{D-2} W^2(R) \sim \left(\sqrt{n_I R^D}\right) V_0\rho_0 W(R) \tag{11}$$

$$\Rightarrow W(R) \sim \left(\frac{V_0\rho_0 n_I^{1/2}}{C}\right) R^{(4-D)/2} \tag{12}$$

For $D < 4$, $W(R)$ grows algebraically with R, tempting one to conclude that the system is short-range-ordered for arbitrarily small disorder strength. A length scale for the short range order was estimated as the length R_0 at which $W(R_0) \sim \pi$, the maximum value for the fluctuation. From Eq. (12), an estimate for this length scale R_0 (also known as the Fukuyama-Lee length [30]) is given by

$$R_0 = \left(\frac{C}{V_0\rho_0 n_I^{1/2}}\right)^{2/(4-D)} \tag{13}$$

R_0 is also a length scale that highlights the breakdown of the above scaling argument. At these length scales, $\phi(\vec{r})$ is large and inconsistent with the linear approximation in Eq. (9). The full periodic nature of the potential needs to be considered to understand the fluctuations beyond R_0.

Nattermann's scaling: Retaining the periodic nature of the potential energy in Eq. (8), we can now get the new scaling estimate for the magnitude of potential energy in a volume R^D as follows. Each impurity contributes to the potential energy by a magnitude $V_0\rho_0\left|\cos(\vec{q}_c.\vec{r}_i + \phi(\vec{r}_i))\right| \sim V_0\rho_0 e^{-\overline{\langle\phi^2(\vec{r}_i)\rangle}/2}$. In a volume R^D, since the typical position $|\vec{r}_i| \sim R$, $V_0\rho_0 e^{-\overline{\langle\phi^2(\vec{r}_i)\rangle}/2} \sim V_0\rho_0 e^{-W^2(R)/2}$, and the total potential energy (PE) thus scales as

$$\mathrm{PE} \sim \left(\sqrt{n_I R^D}\right) V_0\rho_0 e^{-W^2(R)/2} \tag{14}$$

where the factor $\sqrt{n_I R^D}$ follows from fluctuations of $n_I R^D$ independent random impurities.

Equating the elastic energy cost [Eq. (7)] to potential energy gain [Eq. (14)] gives the optimal $W(R)$ given by

$$CR^{D-2}W^2(R) \sim \left(\sqrt{n_I R^D}\right) V_0\rho_0 e^{-W^2(R)/2} \tag{15}$$

$$\Rightarrow W^2(R) \sim (4-D)\log(R/R_0) + \mathcal{O}\left(\log(\log(R/R_0))\right) \tag{16}$$

where R_0 is the same length scale from Eq. (13). Thus for $D < 4$, $W^2(R > R_0)$ grows logarithmically to leading order. This is the Bragg glass order.

Appendix B: Sample preparation and X-ray details

Samples were grown using a Te self-flux method as described in Ref. 32. Small amounts of Pd were included in the melt to produce the palladium intercalated crystals. Crystals produced had an area of 1-2mm across and varied in thickness with intercalation level. Since the CDW transition temperature is well characterized for different intercalation levels, resistivity measurements of the sample batches used were taken to determine the intercalation levels of the samples studied [13]. Samples were shipped to Argonne in sealed vials filled with inert gas and removed and mounted on the tips of polyimide capillaries just before measurement to avoid degradation from water and oxygen exposure. During measurements, samples were cooled using an Oxford N-Helix Cryostream, which surrounded samples with either N_2 or He gas. Measurements were taken with incident x-ray energy of 87 keV in transmission geometry, with samples continuously rotated at $1^\circ\ \mathrm{s}^{-1}$ and a Pilatus 2M CdTe detector taking images at 10 Hz. For each sample at each temperature, three such 365° rotation scans were collected, with the detector slightly offset and the rotation angle slightly changed to fill in detector gaps and allow for removal of detector artifacts (detailed in Ref. 19).

Appendix C: Peak width of a disordered CDW

We describe the relationship between the CDW peak width and the density correlations in a Bragg glass and short-range-ordered phase, following the analysis from Refs. [6, 7, 21]. Consider a 3D lattice with N sites, and atoms arranged at $\vec{r}_n = \vec{R}_n + \vec{c}_n$ where $\vec{R}_n$ are the crystal lattice positions, and $\vec{c}_n$ are the lattice displacements due to a CDW. Let us describe the lattice displacements due to a unidirectional CDW with an incommensurate modulation vector $\vec{q}_c$, given by

$$\vec{c}_n = \vec{c}_0 \cos(\vec{q}_c \cdot \vec{R}_n + \phi_n) \tag{17}$$

where ϕ_n is a non uniform phase with fluctuations due to disorder interaction, and $\vec{c}_0$ is a uniform amplitude (amplitude fluctuations are energetically more expensive, hence neglected). The scattering intensity at a momentum $\vec{Q}$ is given by

$$I(\vec{Q}) = \sum_{n,m} e^{i\vec{Q}\cdot(\vec{R}_n - \vec{R}_m)} \langle e^{i\vec{Q}\cdot(\vec{c}_n - \vec{c}_m)} \rangle_\phi \tag{18}$$

where $\langle \cdots \rangle_\phi$ denotes ensemble average over disordered phase configurations $\{\phi_n\}$, and we assume a uniform disorder averaged form factor set to unity for all atoms. For small $\vec{c}_0$, the $I(\vec{Q})$ is simplified to,

$$\begin{aligned} I(\vec{Q}) &= \sum_{n,m} e^{i\vec{Q}\cdot(\vec{R}_n - \vec{R}_m)} \left[1 - \frac{1}{2} \langle \left(\vec{Q} \cdot (\vec{c}_n - \vec{c}_m) \right)^2 \rangle_\phi \right] + \mathcal{O}(|\vec{Q}\cdot\vec{c}_0|^4) \\ &\approx \sum_{n,m} e^{i\vec{Q}\cdot(\vec{R}_n - \vec{R}_m)} \left[\left(1 - \frac{1}{2}(\vec{Q}\cdot\vec{c}_0)^2 \right) + \frac{1}{4}(\vec{Q}\cdot\vec{c}_0)^2 \left(e^{i\vec{q}_c\cdot(\vec{R}_n - \vec{R}_m)} \langle e^{i(\phi_n - \phi_m)} \rangle_\phi + e^{-i\vec{q}_c\cdot(\vec{R}_n - \vec{R}_m)} \langle e^{-i(\phi_n - \phi_m)} \rangle_\phi \right) \right] \end{aligned}$$

From the above expression, we can deduce the two CDW satellite peaks at $\vec{Q} = \vec{G} \pm \vec{q}_c$ around each Bragg peak at $\vec{G}$. Focusing on the satellite peak around $\vec{G} + \vec{q}_c$, the intensity profile is given by

$$I(\vec{Q} = \vec{G} + \vec{q}_c + \delta\vec{q}) = \frac{1}{4}(\vec{Q}\cdot\vec{c}_0)^2 \sum_{n,m} e^{i\delta\vec{q}\cdot(\vec{R}_n - \vec{R}_m)} \langle e^{-i(\phi_n - \phi_m)} \rangle_\phi \tag{19}$$

where $|\delta\vec{q}| \ll |\vec{q}_c|$. The density correlations $\langle e^{-i(\phi_n - \phi_m)} \rangle_\phi$, which using the Gaussian approximation for small fluctuations get simplified to,

$$\langle e^{-i(\phi_n - \phi_m)} \rangle_\phi = e^{-\frac{1}{2}\langle(\phi_n - \phi_m)^2\rangle_\phi} + \mathcal{O}[\langle(\phi_n - \phi_m)^4\rangle_\phi]. \tag{20}$$

Due to translational symmetry of the disorder averaged phase fluctuations, we can define the density correlation function in terms of fluctuations relative to a reference point, given by

$$C_\phi(\vec{r}) = e^{-\frac{1}{2}\langle(\phi(\vec{r}) - \phi(0))^2\rangle_\phi}, \tag{21}$$

where $\phi(\vec{r}=\vec{R}_n)\equiv\phi_n$. Substituting Eq. (20) and (21) in Eq. (19), we get the CDW satellite intensity as

$$I(\vec{Q}=\vec{G}+\vec{q}_c+\delta\vec{q})\approx\frac{1}{4}(\vec{Q}\cdot\vec{c}_0)^2Nv^{-1}\int(d^3\vec{r})e^{i\delta\vec{q}\cdot\vec{r}}C_\phi(\vec{r}) \tag{22}$$

where we have replaced the discrete lattice sum with an integral over $\vec{r}\equiv\vec{R}_n-\vec{R}_m$, and v^{-1} is the volume of a unit cell. The profile of the CDW peak is thus determined by $C_\phi(\vec{r})$, whose long distance behavior distinguishes long-range-ordered, Bragg glass, and short-range-ordered CDW phases.

1. **Long range ordered CDW**: $C_\phi(\vec{r}\to\infty)\neq 0$ for a CDW with perfect long range ordered phase. Here, Eq. (22) gives delta function peaks with ideally zero peak width.

2. **Short range ordered CDW**: When $C_\phi(\vec{r})\sim e^{-r/\zeta}$, with a correlation length ζ, Eq. (22) gives a broadened (nearly Lorentzian) peak at $\vec{Q}=\vec{G}\pm\vec{q}_c+\delta\vec{q}$ given by

$$I(\vec{Q})\propto(\vec{Q}\cdot\vec{c}_0)^2\zeta^3\frac{1}{\left(1+\zeta^2|\delta\vec{q}|^2\right)^2} \tag{23}$$

whose full width at half maxima (FWHM) is $(2\sqrt{\sqrt{2}-1})\zeta^{-1}$. Thus the observed peak width is determined by the inverse phase correlation length ζ^{-1}, and is independent of the momentum $\vec{Q}$ of the peak.

3. **Bragg glass ordered CDW**: A Bragg glass phase is distinguished by a power law decaying phase correlation: $C_\phi(r>R_0)\sim(r/R_0)^{-\eta}$ where $\eta\approx 1$ in 3D is a universal exponent as shown by Refs. [2, 4], and R_0 is a small distance cut-off [see Eq. 13] that sets the onset of power law decay. For the Bragg glass, Eq. (22) in the limit $|\delta\vec{q}|\to 0$ can be solved to get the intensity at $\vec{Q}=\vec{G}\pm\vec{q}_c+\delta\vec{q}$ as

$$I(\vec{Q})\propto\left(|\delta\vec{q}|^{\eta-3}\right)(\vec{Q}\cdot\vec{c}_0)^2R_0^\eta \tag{24}$$

For 3D, with $\eta=1$ as shown in Ref [2, 4], the peak intensity of a Bragg glass diverges as $|\delta\vec{q}|^{-2}$. As with long range order, the observed width will be the resolution limit of the detector [7].

Appendix D: Disorder pinning and asymmetry

Here we show that the presence of an asymmetry between the satellite peak intensities signals the disorder pinning of lattice modulations. The derivation below follows from Refs [21, 25]. While the asymmetry signature was experimentally observed for short range ordered CDW materials [20, 21, 33], they were also predicted to occur in Bragg glass ordered CDW in Ref. [6, 7].

Consider a 3D lattice with atoms arranged at $\vec{r}_n=\vec{R}_n+\vec{u}_n$ where $\vec{R}_n$ are the crystal lattice positions and $\vec{u}_n$ is a displacement from the n^{th} lattice site. The Fourier component of the displacement modulation is given by

$$\vec{u}_{\vec{q}} = N^{-1/2} \sum_n \vec{u}_n e^{-i\vec{q}\cdot\vec{R}_n} \tag{25}$$

where N is the total number of sites. Let us model the intercalation (disorder) as modifying the original form factor to a new value f_j at random sites j. The Fourier component of the modulated form factor is given by

$$\tilde{f}_{\vec{q}} = N^{-1/2} \sum_n f_n e^{-i\vec{q}\cdot\vec{R}_n}. \tag{26}$$

The scattering intensity at a momentum $\mathcal{Q}$ for this model with intercalation disorder and small lattice displacements is given by

$$\begin{aligned} I(\vec{Q}) &= \sum_{n,m} e^{i\vec{Q}\cdot(\vec{R}_n-\vec{R}_m)} \langle f_n f_m e^{i\vec{Q}\cdot(\vec{u}_n-\vec{u}_m)}\rangle & (27) \\ &= \sum_{n,m} e^{i\vec{Q}\cdot(\vec{R}_n-\vec{R}_m)} \langle f_n f_m \left[1 + i\vec{Q}\cdot(\vec{u}_n-\vec{u}_m)\right]\rangle + \mathcal{O}\left(|\vec{Q}\cdot(\vec{u}_n-\vec{u}_m)|^2\right) & (28) \end{aligned}$$

where $\langle\cdots\rangle$ denotes thermal and disorder average.

We are interested in the asymmetry of the intensities $I(\vec{Q})$ between the two satellite points $\vec{G}\pm\vec{q}$ across a Bragg peak at $\vec{G}$, where $\vec{q}$ is within the first Brillouin zone. Substituting the inverse Fourier transforms of Eq. (25) for $\vec{u}_i$ and Eq. (26) for f_i in to Eq. (28), we get the satellite asymmetry to be

$$I(\vec{G}+\vec{q}) - I(\vec{G}-\vec{q}) = 2i\tilde{f}_0\vec{G}\cdot\left(\langle\vec{u}_{-\vec{q}}\tilde{f}_{\vec{q}}\rangle - \langle\vec{u}_{\vec{q}}\tilde{f}_{-\vec{q}}\rangle\right) + \mathcal{O}\left(|\vec{G}\cdot\vec{u}_{\vec{q}}|^2\right) \tag{29}$$

where $N^{-1/2}\tilde{f}_0 = N^{-1}\sum_j f_j$ is the average form factor of the disordered lattice. If the lattice displacement modulations are not correlated with the intercalant positions (no disorder pinning), then the term $\langle\vec{u}_{\vec{q}}\tilde{f}_{-\vec{q}}\rangle = \langle\vec{u}_{\vec{q}}\rangle\langle\tilde{f}_{-\vec{q}}\rangle = 0$ since $\langle\vec{u}_{\vec{q}}\rangle = \langle\vec{u}_{-\vec{q}}\rangle = 0$. The $\langle\vec{u}_{\vec{q}}\rangle = 0$ is true for both incommensurate long range ordered CDW (since the CDW phase in each disorder configuration is arbitrary) and for short range ordered displacements (the disorder average of the displacements is zero). Thus the leading order contribution to the intensity asymmetry is zero in the absence of disorder pinning of lattice modulations.

On the other hand, in the presence of disorder pinning, $\langle\vec{u}_{\vec{q}}\tilde{f}_{-\vec{q}}\rangle \neq \langle\vec{u}_{\vec{q}}\rangle\langle\tilde{f}_{-\vec{q}}\rangle$ and hence not trivially 0. To explicitly see this non-vanishing of satellite asymmetry from disorder pinning, we discuss a simple model put forward in Ref. [33]. Consider a single impurity at a random site $\vec{R}_0$ that interacts with the charge density such that the phase of the charge density is fixed to a value ϕ_0 at site $\vec{R}_0$. The pinned CDW is given by $\rho_n = \rho_0 \sin\left[\vec{q}_c\cdot(\vec{R}_n-\vec{R}_0)+\phi_0\right]$. The lattice modulations are in quadrature with the CDW and is given by $\vec{u}_n = \vec{u}_0\cos\left[\vec{q}_c\cdot(\vec{R}_n-\vec{R}_0)+\phi_0\right]$. Taking f_I as the atomic form factor of the impurity and f_0 as that of the pure atom, the satellite asymmetry [Eq. (29)] for this single impurity pinning gives,

$$I(\vec{G}+\vec{q}) - I(\vec{G}-\vec{q}) = 2N^{-1/2} f_0 (f_I - f_0)(\vec{G}\cdot\vec{u}_0)\sin(\phi_0) \tag{30}$$

A maximum asymmetry is when $(f_I - f_0)\sin(\phi_0) = 1$ which corresponds to the CDW having a maximum or minimum over the impurity depending on whether the interaction is attractive or repulsive. This picture describes strong pinning, where the CDW is pinned to a constant phase ϕ_0 above each impurity. However, the pinning for a Bragg glass is weak, where the phase is modulated by the collective interaction of impurities. A calculation of the asymmetry for Bragg glass was carried out in Refs. 6 and 7, and was shown to be an experimentally observable effect in principle.

Appendix E: Momentum dependence of CDW Peak width

In addition to the phase fluctuations that destroy long range CDW order, displacement of atoms from their ideal lattice sites (displacement fluctuations) that destroy long range lattice order will also contribute to the broadening of the CDW peaks. Here we show that the width due to displacement fluctuations is momentum ($\vec{Q}$) dependent, in contrast to the $\vec{Q}$ independent broadening due to CDW phase fluctuations. Our model is similar to that of a paracrystal [chapter. 9 of Ref.[25]], with the modification of introducing a CDW with phase fluctuations on top of the lattice displacements. Using the same 3D lattice with N sites as in Appendix-B, but with an additional lattice displacement $\vec{u}_n$ that can arise from thermal vibrations or disorder interaction, the atoms are arranged at $\vec{r}_n = \vec{R}_n + \vec{c}_n + \vec{u}_n$ where $\vec{R}_n$ are the lattice sites and $\vec{c}_n$ are the CDW displacements. The scattering intensity at a momentum $\vec{Q}$ [Eq. (18)] is modified for the disordered lattice as,

$$I(\vec{Q}) = \sum_{n,m} e^{i\vec{Q}\cdot(\vec{R}_n-\vec{R}_m)} \langle e^{i\vec{Q}\cdot(\vec{c}_n-\vec{c}_m)}\rangle_\phi \langle e^{i\vec{Q}\cdot(\vec{u}_n-\vec{u}_m)}\rangle_u \tag{31}$$

where $\langle\cdots\rangle_u$ denotes ensemble average over lattice displacement configurations $\{u_n\}$, and we have assumed the lattice displacements are uncorrelated with the phase fluctuations. The CDW intensity around $\vec{Q} = \vec{G} + \vec{q}_c$ in Eq. (19) is now modified to

$$I(\vec{Q} = \vec{G} + \vec{q}_c + \delta\vec{q}) = \frac{1}{4}(\vec{Q}\cdot\vec{c}_0)^2 \sum_{n,m} e^{i\delta\vec{q}\cdot(\vec{R}_n-\vec{R}_m)} \langle e^{-i(\phi_n-\phi_m)}\rangle_\phi \langle e^{-i\vec{Q}\cdot(\vec{u}_n-\vec{u}_m)}\rangle_u \tag{32}$$

where the factor $\langle e^{-i\vec{Q}\cdot(\vec{u}_n-\vec{u}_m)}\rangle_u$ under the Gaussian approximation gives

$$\langle e^{-i\vec{Q}\cdot(\vec{u}_n-\vec{u}_m)}\rangle_u = e^{-\frac{1}{2}\langle(\vec{Q}\cdot(\vec{u}_n-\vec{u}_m))^2\rangle_u} + \mathcal{O}[\langle(\vec{Q}\cdot(\vec{u}_n-\vec{u}_m))^4\rangle_u]. \tag{33}$$

where $\langle(\vec{Q}\cdot(\vec{u}_n-\vec{u}_m))^2\rangle_u$ quantify the mean squared fluctuations in relative lattice displacements. Defining a correlation function $C_u(\vec{r},\vec{Q})$ for the displacements relative to a reference point given by,

$$C_u(\vec{r},\vec{Q}) = e^{-\frac{1}{2}\langle\left(\vec{Q}\cdot(\vec{u}(\vec{r})-\vec{u}(0))\right)^2\rangle_u}, \tag{34}$$

where $\vec{u}(\vec{R}_n)\equiv\vec{u}_n$, the CDW peak intensity in Eq. (22) is modified to,

$$I(\vec{Q}=\vec{G}+\vec{q}_c+\delta\vec{q}) \approx \frac{1}{4}(\vec{Q}\cdot\vec{c}_0)^2 N v^{-1}\int(d^3\vec{r})e^{i\delta\vec{q}\cdot\vec{r}}C_\phi(\vec{r})C_u(\vec{r},\vec{Q}) \tag{35}$$

What sets the displacement fluctuations apart from CDW phase fluctuations is the $\vec{Q}$ dependence of $C_u(\vec{r},\vec{Q})$. It is this distinction that leads to the $\vec{Q}$ dependent broadening signature for the displacement fluctuations. To see this, consider an exponentially decaying form for the displacement correlation given by $C_u(\vec{r},\vec{Q}) \sim e^{-|\vec{Q}|^2(\gamma_u r)}$. Here γ_u with dimensions of length can be interpreted as the root mean square value of the relative displacement between neighboring atoms. When combined with the short range phase correlation $C_\phi(\vec{r}) \sim e^{-r/\zeta_\phi}$, Eq. (35) gives an approximately Lorentzian peak profile at $\vec{Q}=\vec{G}\pm\vec{q}_c+\delta\vec{q}$ given by

$$I(\vec{Q}) \propto \frac{1}{\left(1+\dfrac{|\delta\vec{q}|^2}{(\zeta_\phi^{-1}+|\vec{Q}|^2\gamma_u)^2}\right)^2} \tag{36}$$

whose full width at half maxima (FWHM) is given by

$$\text{FWHM} \propto \zeta_\phi^{-1}+|\vec{Q}|^2\gamma_u \tag{37}$$

This shows the quadratic in momentum broadening due to displacement fluctuations. While the above form was obtained for a simple displacement correlation function that decay isotropically, a more general form for the broadening would be

$$\text{FWHM} \propto \zeta_\phi^{-1}+\gamma_H Q_H^2+\gamma_K Q_K^2+\gamma_L Q_L^2 \tag{38}$$

and we do not include terms like $Q_H Q_K$ etc. as they violate the reflection symmetry of the lattice. From a quadratic fit to the momentum dependence of the FWHM, the contribution from phase fluctuations: ζ_ϕ^{-1} can be extracted as the intercept.

Numerical illustration of momentum dependent peak broadening: To complement the above derivation, we numerically calculate the scattering intensity [Eq. (31)] for a 1D lattice model with short range ordered CDW phase and lattice displacements.

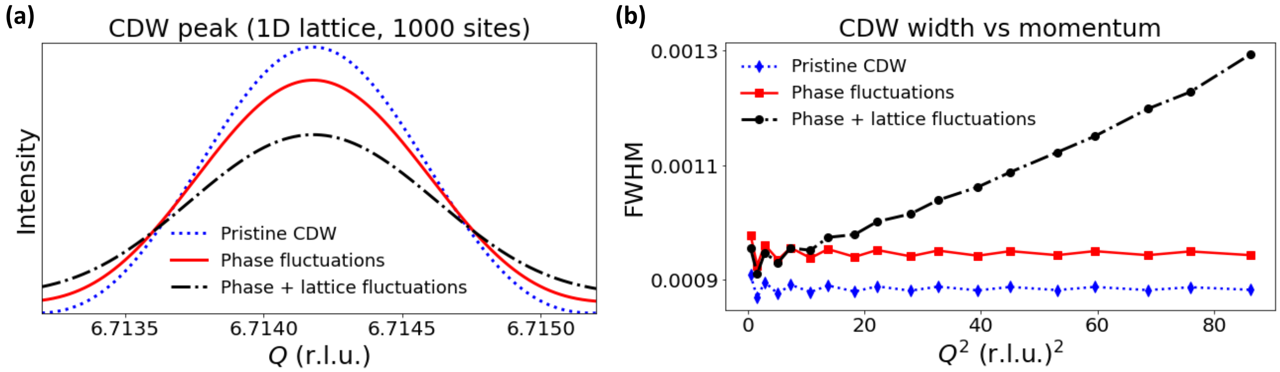

FIG. 1. **(a):** Numerically calculated intensity of a CDW peak, and **(b):** the momentum (Q) dependence of the full width at half maxima (FWHM) of the CDW peaks, in a 1D lattice with 1000 sites. The intensities are calculated for three disorder configurations: (1) pristine CDW with no disorder, (2) CDW with only phase fluctuations and (3) CDW with both phase and lattice fluctuations. Both configurations (2) and (3) lead to a broadening of the peak [panel(a)]. However, the FWHM remains independent of Q for the configuration with only phase fluctuations, while the FWHM for the configuration with both phase and lattice fluctuations show a Q^2 dependence. From the intercept of the Q^2 dependent FWHM, we can isolate the broadening contribution of the phase fluctuations.

On a lattice with 1000 sites, we set the CDW modulation $q_c = 2/7$ to mimic the CDW of RTe$_3$, and set the CDW amplitude $= 0.01$. To generate a disordered phase configuration with short range correlation $C_\phi(|n-m|) \sim e^{-|n-m|/\zeta_\phi}$ between sites n and m, we start with the $n = 0$ site where $\phi_0 = 0$ and the phases ϕ_n for each site $n > 0$ are selected as $\phi_n = \phi_{n-1} + d\phi$ where $d\phi$ is drawn from a normal distribution with zero mean and standard deviation σ_ϕ (=0.025). This distribution generates phases whose mean square fluctuations are given by $\langle(\phi_n - \phi_m)^2\rangle_\phi = |n-m|\sigma_\phi^2$, and the phase correlation [Eq. (21)] given by $C_\phi(|n-m|) = e^{-|n-m|\sigma_\phi^2/2}$. Similarly, to generate a short ranged lattice displacement configuration, the lattice displacements u_n are generated as $u_n = u_{n-1} + du$ where du is drawn from a normal distribution with zero mean and standard deviation σ_u (=0.001), starting with $u_0 = 0$. This generates displacement configurations with mean squared fluctuation $\langle(u_n - u_m)^2\rangle_u = |n-m|\sigma_u^2$. We generate 400 realizations of phase and displacement configurations and calculate the intensity using Eq. (31).

We show the calculated intensity profile of a CDW peak and the momentum (Q) dependence of the peak width in SM Fig. 1. We see that while a short range ordered phase broadens the CDW peak whose width is independent of Q, a short range ordered lattice leads to broadening that is proportional to Q^2. In the presence of both short range ordered phase and lattice displacements, the Q independent broadening due to phase only disorder can be extracted from the intercept of the Q^2 broadening.

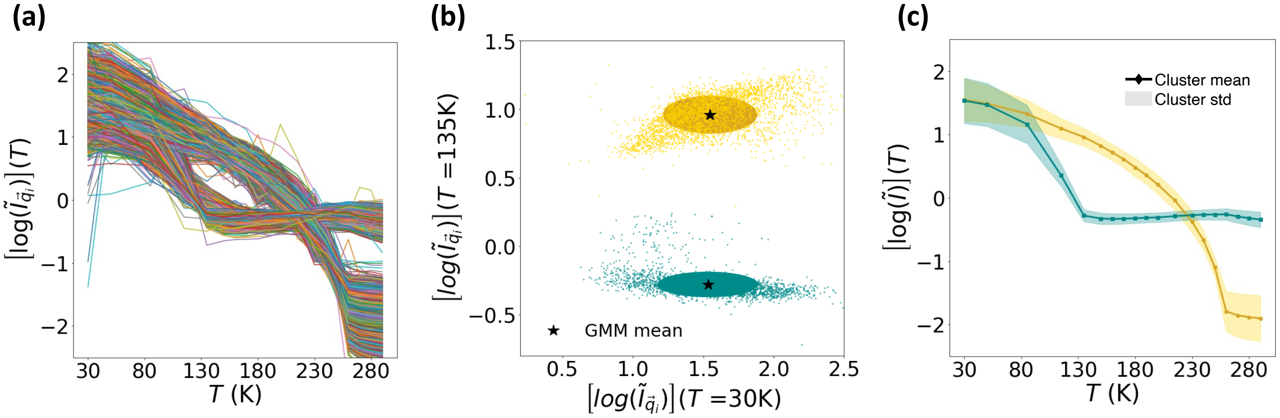

FIG. 2. A simplified illustration of *X-TEC* to cluster distinct intensity-temperature trajectories, $I(T)$, given the collection of series $\{I_{\vec{q}}(T_1), I_{\vec{q}}(T_2), \ldots, I_{\vec{q}}(T_d)\}$ ($d = 19$ in this figure) at various momentum $\vec{q}$ in the reciprocal space. The raw trajectories rescaled as $\log[\tilde{I}_{\vec{q}}(T_i)] = \log[I_{\vec{q}}(T_i)] - \langle\log[I_{\vec{q}}(T_i)]\rangle_T$ [panel (a)] can be mapped to a simple Gaussian Mixture Model (GMM) clustering problem on a d-dimensional space, whose 2D projection (along $T = 30$K and $T = 135$K) is shown in panel (b). The GMM identifies two distinct clusters and assigns them different colors. From the cluster means (star symbol) and standard deviations (colored ellipsoids) of the GMM [panel (b)], we get the distinct trajectories of $\log[\tilde{I}(T)]$ and their standard deviation, with colors reflecting their cluster assignments [panel (c)].

Appendix F: X-ray Temperature Clustering: *X-TEC*

The underlying principle of *X-TEC* is to identify the distinct temperature trajectories through a Gaussian mixture model clustering [12]. In SM-Fig. 2, we show a simplified illustration of the GMM in action. A collection of raw intensity-temperature trajectories [SM-Fig. 2(a)] given by $\{I_{\vec{q}}(T_1), I_{\vec{q}}(T_2), \ldots, I_{\vec{q}}(T_d)\}$ at various momenta $\vec{q}$ in reciprocal space can be represented as a distribution of points in a d dimensional hyperspace, whose axis spans the intensities at each temperature. For visualization, a 2D cross section of this hyper space is shown in SM-Fig. 2(b). The figure shows that the points are separated into two distinct groups (clusters). A Gaussian Mixture Model (GMM) clustering classifies these points into different clusters and assigns a mean and standard deviation for each cluster. The cluster means reveal the distinct temperature trajectories in the data [SM-Fig. 2(c)], while the standard deviation shows that the clusters are well separated. In this example, a visual inspection of the raw intensities as well as a 2D projection can already reveal the distinct clusters. However the real data is more messy [See Fig. 1(e)], and requires a GMM clustering on the entire hyperspace to identify the distinct trajectories.

Appendix G: Conventional peak width analysis

The conventional approach of extracting the peak width would be to take one-dimensional line cuts through CDW peaks in the binned data and extract intensity and width parameters from fitting. Fitting domains must be chosen

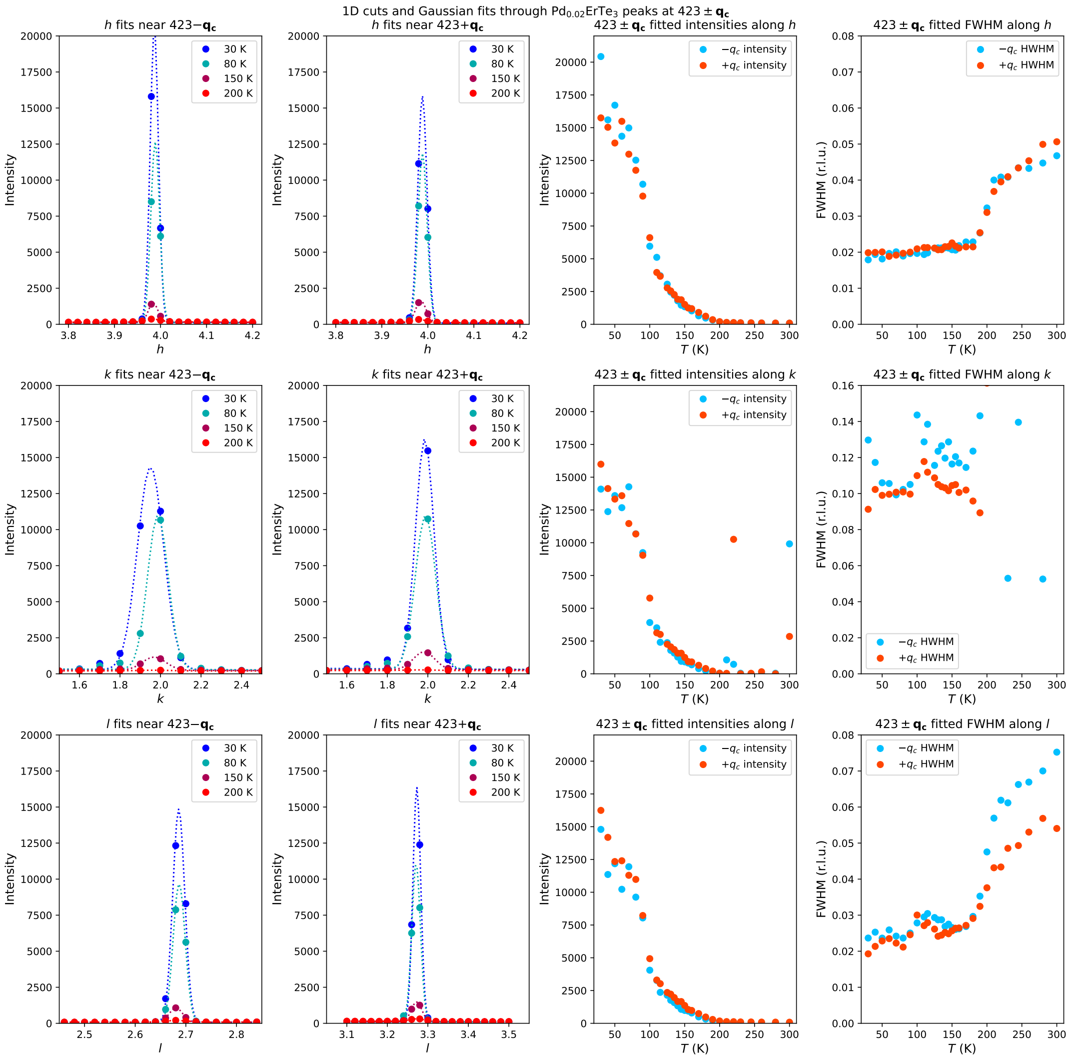

FIG. 3. A set of three one-dimensional Gaussian functions can be used to fit superstructure peaks and extract intensity and width parameters to characterize peaks. This approach is applied here to the $432 \pm \mathbf{q}_c, \mathbf{q}_c \approx \frac{2}{7}\mathbf{c}^*$ superstructure peaks in Pd$_{0.02}$ErTe$_3$. For all rows, the left two figures are cuts taken through superstructure peaks, with circles indicating data and dotted lines representing fitted Gaussians; the right two figures are fitted parameters at different temperatures. **Top row**: Line cuts taken along h.**Middle row**: Line cuts taken along k. Note that the peak become so broad along k above $T \approx 210$ K that the fitting function fails. **Bottom row**: Line cuts taken along l. It is notable that the full-width half maximum (FWHM) of the fit approaches the bin width at low temperatures, indicating that the peak is resolution-limited.

arbitrarily in relation to diffuse scattering and spurious crystallographic imperfections, making this approach difficult to apply to the entire dataset. Moreover, the necessity of determining the goodness of fit makes this approach impractical to scale. Applying this approach to an ad-hoc choice of peaks at $hkl = 4\ 2\ 3 \pm q_c$ in SM Fig. 3 shows that the spurious signals make it difficult to find a uniform way to fit even a small number of peaks in these data, and even the best-fitted parameters will have low precision.

Appendix H: Peak spread analysis with *X-TEC*

In this section, we first provide details of the steps to extract the peak spread $\Gamma_{\vec{q}}(T)$ [Eq. (1)] from the XRD data and benchmark them with line cuts on selected CDW-1 peaks [SM Fig. 4]. We then show the underlying quadratic momentum dependence of $\Gamma_{\vec{q}}$, and the extraction of the $\vec{q}$ independent term Γ_0 that quantifies the broadening purely due to CDW phase fluctuations [SM Fig. 5].

1. Benchmarking peak spread

The conventional approach to extract a FWHM is shown for a CDW-1 peak at the three levels of intercalation in SM Fig. 4 (a), (f) and (k). Our high throughput measure $\Gamma_{\vec{q}}$ [Eq. (1)] directly provides a measure for the spread of the peak (in units of the number of pixels). This is achieved by using *X-TEC* to identify the connected pixels whose intensity trajectories belong to the CDW order parameter cluster. This is shown in SM Fig. 2 (b), (g) and (l), where the red boundary determined by *X-TEC* marks the extent of the CDW peaks. We quantify the spread of this CDW peak (centered at momentum $\vec{q}$) with $\Gamma_{\vec{q}}$ which is the ratio of the total intensity inside the peak boundary to the maximum intensity of the peak. We restrict to the in-plane peak spread with intensities at integer K values of the out of plane (b^*) axis, to avoid the lower resolution along b^* axis [0.1 (r.l.u.) compared to 0.02 (r.l.u.) for the in-plane] from limiting the overall resolution of the spread. The estimated $\Gamma_{\vec{q}}$ is compared with the FWHMs of the line cuts in SM Fig. 2 (c), (h) and (m). We see that the $\Gamma_{\vec{q}}$ faithfully captures the features of the FWHMs, in particular, the rapid onset of broadening above a transition temperature.

However, both the FWHMs and the $\Gamma_{\vec{q}}$ show an erratic temperature trajectory, reflecting the errors in the width estimation from the small resolution peaks (the peaks are roughly spread over 2-3 pixels). Collecting all $\Gamma_{\vec{q}}$ with $\vec{q}$ spanning ~ 2000 peaks, we find a wide variation in the range of values for the spread, [see SM Fig. 2 (d), (i) and (n)]. Buried under these seemingly erratic trajectories is the systematic $\vec{q}$ dependence from lattice distortions [see SM Fig. 5] and the unique $\vec{q}$ independent spread Γ_0 of the disordered CDW [see Fig. 3 of main text].

An important step in the estimation of $\Gamma_{\vec{q}}$ is the removal of the background intensity offset from the CDW peak intensities. This background contribution is estimated as the average of the intensities outside the CDW boundary in a 10x10 pixel neighborhood of the peak [the blue region outside the red boundary in SM Fig. 4 (b), (g) and (l)], and this offset contribution is subtracted from the total and maximum intensity of the CDW peak before estimating Γ_q. In SM Fig. 4 (e), (j) and (o), we show the effect of not removing the background offset on the Γ_0. Keeping the

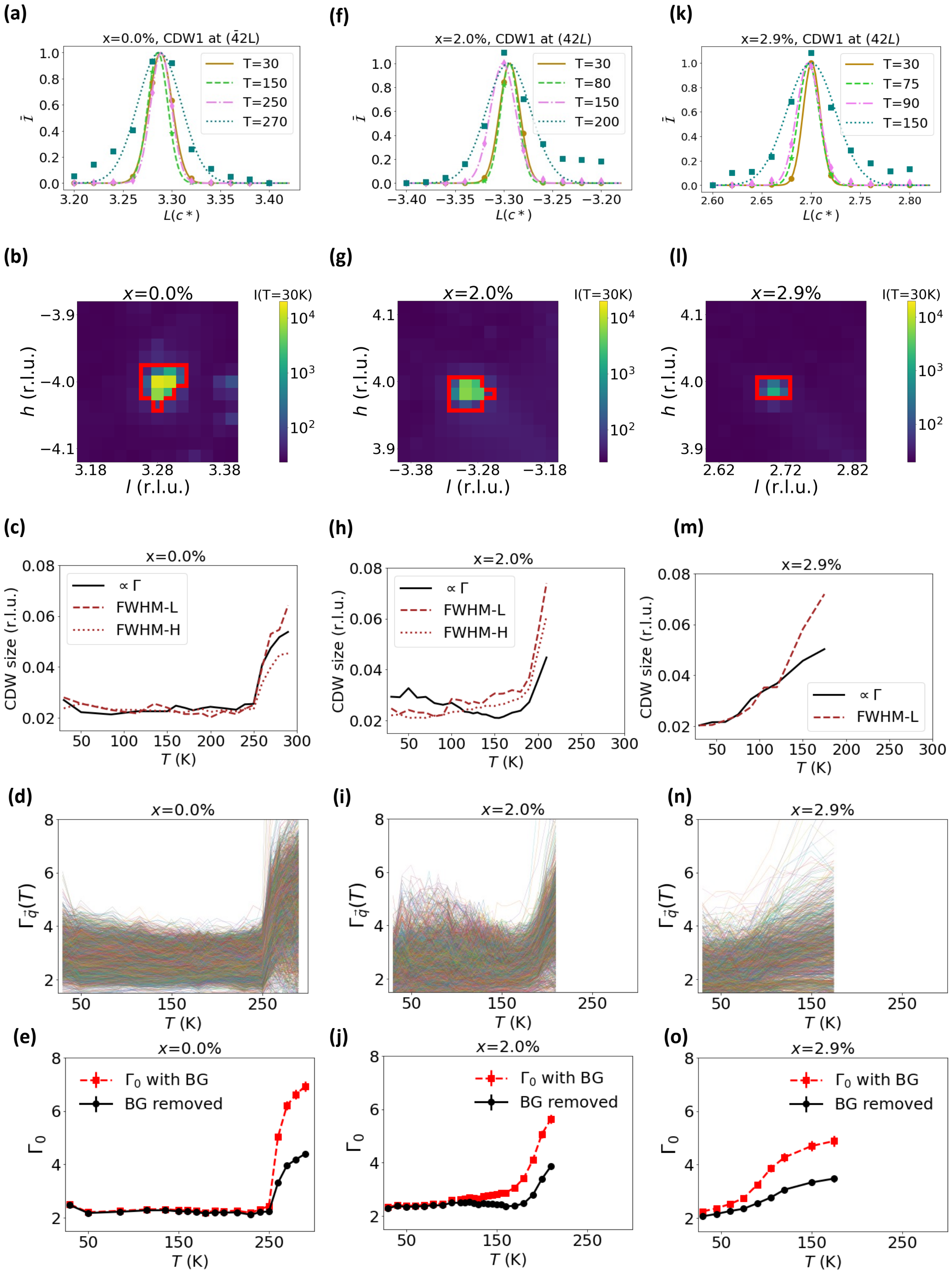

FIG. 4. Extracting and benchmarking the peak spread. **(a):** Line cut along a CDW-1 peak at various temperatures T for the pristine sample ($x = 0\%$). The intensities (symbols) are averaged along $H = \bar{4} \pm 0.02$ r.l.u and $K = 2$, and normalized with its maximum value at the peak. The minimum intensity in the line cut is subtracted to remove any background offset. The lines are Gaussian fits. **(b):** The intensity of the CDW-1 peak in the $K = 2$ plane [same peak as in (a)] at $T = 30$K, with the *X-TEC* determined peak boundaries (red contour) for the $x = 0\%$. **(c):** The peak spread (Γ) [Eq. (1)] for the CDW peak in (a-b), along with the FWHM from line cuts along H (FWHM-H) and L (FWHM-L), at various T for $x = 0\%$. **(d):** The T trajectory of the peak spread ($\Gamma_{\vec{q}}$) of 2778 CDW-1 peaks in the $x = 0\%$ data (thin colored lines). **(e):** Comparing Γ_0 with the background intensity offset removed (BG removed), and Γ_0 keeping the background offset (Γ_0 with BG). Lines are guides to the eyes. **(f-j):** Same as panels (a-e) respectively but for $x = 2\%$ intercalated sample. The panel (i) shows $\Gamma_{\vec{q}}$ of 1986 peaks (thin colored lines). **(k-o):** Same as panels (f-j) but for $x = 2.9\%$ intercalated sample. Panel (n) shows $\Gamma_{\vec{q}}$ of 1440 peaks.

background intensity results in an overestimation of the spread, especially at higher temperatures where the peak height is smaller. This is because the peak spread measure misinterprets the extra background intensity outside the true peak as a genuine broadening of the peak.

2. Momentum dependence of peak spread

In SM Fig. 5, we show that the spread $\Gamma_{\vec{q}}$ in the XRD data has a systematic broadening with quadratic dependence in $\vec{q}$ as predicted in Appendix-E. To simplify the visualization of the 3D quadratic fit in Eq. (2), we project the momentum dependence of $\Gamma_{\vec{q}}$ to one direction by averaging over the other directions. We show the H^2 dependence of $\Gamma_{\vec{q}}$ in SM Fig. 5 (a), and the L^2 dependence in (c) and (e), for the three levels of intercalation. The $\Gamma_{\vec{q}}$ fits well with the quadratic function.

The full 3D fit of $\Gamma_{\vec{q}}$ using Eq. (2) extracts the quadratic coefficients γ_H, γ_K, γ_L as well as the momentum-independent intercept Γ_0. While Γ_0 is reported in the main text [Fig. 3 (c-f)], in SM Fig. 5 (b), (d) and (f) we report their respective γ_H, γ_K, and γ_L values.

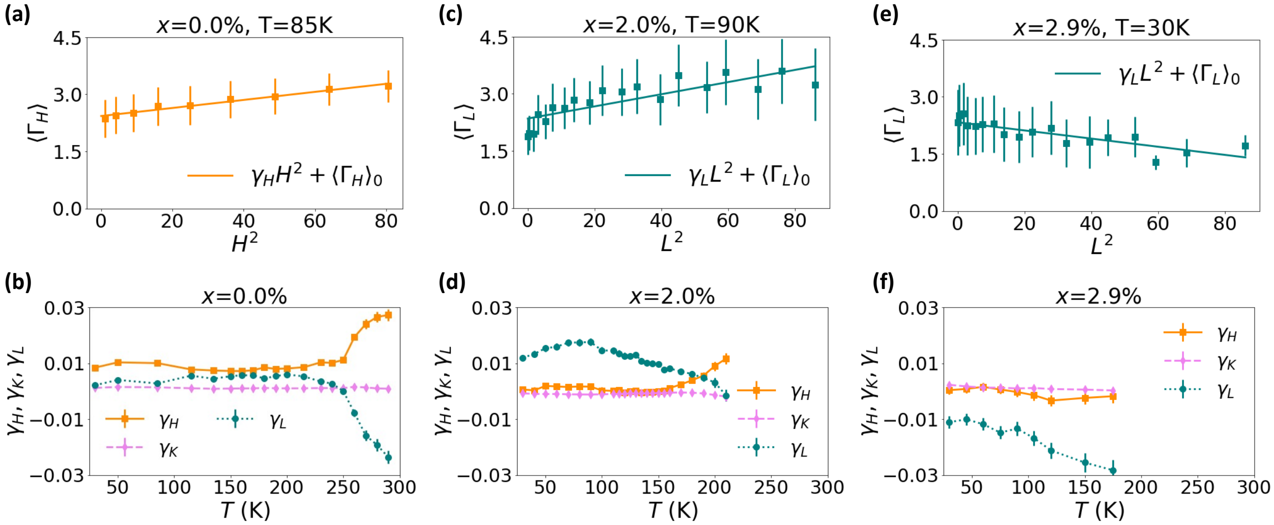

FIG. 5. **(a)**: The H^2 dependence of the peak spread in the $x = 0\%$ sample at T=85K. The $\langle\Gamma_H\rangle$ (symbols) is the spread obtained by averaging $\Gamma_{\vec{q}}$ over K and L that share the same $|H|$. The error bars indicate standard deviation of $\Gamma_{\vec{q}}$ at $|H|$. The fit: $\gamma_H H^2 + \Gamma_0$ agrees well with $\langle\Gamma_H\rangle$ within the error bars. **(b)**: The momentum coefficients γ_H, γ_K, γ_L from the 3D quadratic fit [Eq. (2) of main text] to $\{\Gamma_{\vec{q}}\}$ at various temperatures for the $x = 0\%$. The lines are guides to the eye. **(c)**: Same as (a) but for the L^2 dependence of the spread, $\langle\Gamma_L\rangle$ (symbols) (by averaging $\Gamma_{\vec{q}}$ over H and K at $|L|$) for the $x = 2\%$ intercalated sample at T=90K. The fit $\gamma_L L^2 + \langle\Gamma_L\rangle_0$ also agrees well within the standard deviation of $\Gamma_{\vec{q}}$ at L. **(d)**: Same as (b), but for the $x = 2\%$ intercalated sample. **(e-f)** Same as (c-d) respectively, but for $x = 2.9\%$ intercalated sample.

[1] "The Nobel Prize in Physics 2021," https://www.nobelprize.org/prizes/physics/2021/parisi/lecture/.

[2] Thierry Giamarchi and Pierre Le Doussal, "Elastic theory of flux lattices in the presence of weak disorder," Physical Review B **52**, 1242–1270 (1995).

[3] Thomas Nattermann, "Scaling approach to pinning: Charge density waves and giant flux creep in superconductors," Phys. Rev. Lett. **64**, 2454–2457 (1990).

[4] Thierry Giamarchi and Pierre Le Doussal, "Elastic theory of pinned flux lattices," Phys. Rev. Lett. **72**, 1530–1533 (1994).

[5] T. Giamarchi and P. Le Doussal, "Phase diagrams of flux lattices with disorder," Physical Review B **55**, 6577–6583 (1997).

[6] Alberto Rosso and Thierry Giamarchi, "X-ray diffraction of a disordered charge density wave," Physical Review B **68**, 140201 (2003).

[7] Alberto Rosso and Thierry Giamarchi, "X-ray spectrum of a pinned charge density wave," Physical Review B **70**, 224204 (2004).

[8] T. Klein, I. Joumard, S. Blanchard, J. Marcus, R. Cubitt, T. Giamarchi, and P. Le Doussal, "A Bragg glass phase in the vortex lattice of a type II superconductor," Nature **413**, 404–406 (2001).

[9] Jun-ichi Okamoto, Carlos J. Arguello, Ethan P. Rosenthal, Abhay N. Pasupathy, and Andrew J. Millis, "Experimental Evidence for a Bragg Glass Density Wave Phase in a Transition-Metal Dichalcogenide," Physical Review Letters **114**, 026802 (2015).

[10] Alan Fang, Joshua A. W. Straquadine, Ian R. Fisher, Steven A. Kivelson, and Aharon Kapitulnik, "Disorder-induced suppression of charge density wave order: STM study of Pd-intercalated ${\mathrm{ErTe}}_{3}$," Physical Review B **100**, 235446 (2019).

[11] Laimei Nie, Gilles Tarjus, and Steven Allan Kivelson, "Quenched disorder and vestigial nematicity in the pseudogap regime of the cuprates," Proceedings of the National Academy of Sciences **111**, 7980–7985 (2014).

[12] Jordan Venderley, Krishnanand Mallayya, Michael Matty, Matthew Krogstad, Jacob Ruff, Geoff Pleiss, Varsha Kishore, David Mandrus, Daniel Phelan, Lekhanath Poudel, Andrew Gordon Wilson, Kilian Weinberger, Puspa Upreti, Michael Norman, Stephan Rosenkranz, Raymond Osborn, and Eun-Ah Kim, "Harnessing interpretable and unsupervised machine learning to address big data from modern X-ray diffraction," Proceedings of the National Academy of Sciences **119**, e2109665119 (2022).

[13] J. A. W. Straquadine, F. Weber, S. Rosenkranz, A. H. Said, and I. R. Fisher, "Suppression of charge density wave order by disorder in Pd-intercalated ${\mathrm{ErTe}}_{3}$," Physical Review B **99**, 235138 (2019).

[14] Yoseph Imry and Shang-keng Ma, "Random-Field Instability of the Ordered State of Continuous Symmetry," Physical Review Letters **35**, 1399–1401 (1975).

[15] A. M. Hindeleh and R. Hosemann, "Microparacrystals: The intermediate stage between crystalline and amorphous," Journal of Materials Science **26**, 5127–5133 (1991).

[16] Alan Fang, Anisha G. Singh, Joshua A. W. Straquadine, Ian R. Fisher, Steven A. Kivelson, and Aharon Kapitulnik, "Robust superconductivity intertwined with charge density wave and disorder in Pd-intercalated ${\mathrm{ErTe}}_{3}$," Physical Review Research **2**, 043221 (2020).

[17] N. Ru, C. L. Condron, G. Y. Margulis, K. Y. Shin, J. Laverock, S. B. Dugdale, M. F. Toney, and I. R. Fisher, "Effect of chemical pressure on the charge density wave transition in rare-earth tritellurides $R{\mathrm{Te}}_{3}$," Physical Review B **77**, 035114 (2008).

[18] A. A. Sinchenko, P. D. Grigoriev, P. Lejay, and P. Monceau, "Spontaneous breaking of isotropy observed in the electronic transport of rare-earth tritellurides," Phys. Rev. Lett. **112**, 036601 (2014).

[19] Matthew J Krogstad, Stephan Rosenkranz, Justin M Wozniak, Guy Jennings, Jacob P C Ruff, John T Vaughey, and Raymond Osborn, "Reciprocal space imaging of ionic correlations in intercalation compounds," Nature Materials **19**, 63–68 (2020), 1902.03318.

[20] S. Ravy and J. P. Pouget, "Structural studies of the CDW interaction with defects," Le Journal de Physique IV **03**, C2–C2–114 (1993).

[21] S. Ravy, S. Rouzière, J.-P. Pouget, S. Brazovskii, J. Marcus, J.-F. Bérar, and E. Elkaim, "Disorder effects on the charge-density waves structure in V- and W-doped blue bronzes: Friedel oscillations and charge-density wave pinning," Physical Review B **74**, 174102 (2006).

[22] Chen Zeng, P. L. Leath, and Daniel S. Fisher, "Absence of Two-Dimensional Bragg Glasses," Physical Review Letters **82**, 1935–1938 (1999).

[23] Pierre Le Doussal and Thierry Giamarchi, "Dislocations and Bragg glasses in two dimensions," Physica C: Superconductivity **331**, 233–240 (2000).

[24] S. Rouzière, S. Ravy, J.-P. Pouget, and S. Brazovskii, "Friedel oscillations and charge-density wave pinning in quasi-one-dimensional conductors: An x-ray diffraction study," Phys. Rev. B **62**, R16231–R16234 (2000).

[25] A. Guinier, *X-Ray Diffraction: In Crystals, Imperfect Crystals, and Amorphous Bodies* (Dover Publications, New York, 1994).

[26] V. J. Emery and J. D. Axe, "One-dimensional fluctuations and the chain-ordering transformation in hg$_{3-\delta}$Asf$_6$," Phys. Rev. Lett. **40**, 1507–1511 (1978).

[27] I. U. Heilmann, J. D. Axe, J. M. Hastings, G. Shirane, A. J. Heeger, and A. G. MacDiarmid, "Neutron investigation of the dynamical properties of the mercury-chain compound hg$_{3-\delta}$Asf$_6$," Phys. Rev. B **20**, 751–762 (1979).

[28] Richard D. Spal, Cynthia E. Chen, Takeshi Egami, Paul J. Nigrey, and Alan J. Heeger, "X-ray scattering study of

one-dimensional lattice dynamics inhg3-δasf6," Physical Review B **21**, 3110–3118 (1980).

[29] H. Endres, J.P. Pouget, and R. Comes, "Diffuse x-ray scattering and order-disorder effects in the iodide chain compounds n,n'-diethyl-n,n'-dihydrophenazinium iodide, e2pi1.6, and n,n'-diebenzyl-n,n'-dihydrophenazinium iodide, b2pi1.6," Journal of Physics and Chemistry of Solids **43**, 739–748 (1982).

[30] H. Fukuyama and P. A. Lee, "Dynamics of the charge-density wave. I. Impurity pinning in a single chain," Physical Review B **17**, 535–541 (1978).

[31] Michel J. P. Gingras and David A. Huse, "Topological defects in the random-field XY model and the pinned vortex lattice to vortex glass transition in type-II superconductors," Physical Review B **53**, 15193–15200 (1996).

[32] N. Ru and I. R. Fisher, "Thermodynamic and transport properties of yte3, late3 and cete3," Physical Review B **73**, 033101 (2006).

[33] S Ravy, JP Pouget, and R Comes, "Destructive interferences between diffuse scatterings due to disorder and displacive modulation (x-ray "white line" effect)," Journal de Physique I **2**, 1173–1190 (1992).